Enhancing Pair Hopping in a Floquet-Engineered Two-Site Hubbard Model

Simon Bauer

Bachelorarbeit in Physik
angefertigt im Physikalischen Institut

vorgelegt der
Mathematisch-Naturwissenschaftlichen Fakultät
der
Rheinischen Friedrich-Wilhelms-Universität
Bonn

August 2020

Ich versichere, dass ich diese Arbeit selbstständig verfasst und keine anderen als die angegebenen Quellen und Hilfsmittel benutzt sowie die Zitate kenntlich gemacht habe.

Bonn, 23.08.2020 S. Bauer
Datum Unterschrift

1. Gutachterin: Prof. Dr. Corinna Kollath
2. Gutachterin: Dr. Ameneh Sheikhan Soudani

Contents

CHAPTER 1

Introduction

With advances in cooling techniques, neutral atomic gases can now be brought down to temperatures of fractions of a degree above absolute zero. These ultracold gases cannot be described classically but explicitly exhibit quantum-mechanical behaviour, like the formation of Bose-Einstein condensates, an effect proposed by Einstein in 1924-1925 [1] whose first experimental observation led to the 2001 Nobel Prize in physics [2].

When introducing these cold atoms into off-resonant laser light fields, they sense a potential depending on the time-averaged electric field $\mathbf{E}(\mathbf{x})$, due to the Stark effect [3]. By creating standing wave light fields the atoms can be subjected to periodic potentials, so called optical lattices, similar to electrons in the atomic potential wells in a solid. These systems can be described by Hubbard-type Hamiltonians [3], which originated from a simple model for the competition of kinetic and tight-binding interaction energy of electrons in a solid. Within this Fermi-Hubbard model, the electrons can tunnel between the atoms and interact with other electrons on the same atom [4]. While there are various reasons why these electrons only very roughly behave like this, the cold atoms in optical lattices have been found to be very clean realisations of these Hubbard-type models [3]. Because of this, ultracold gases have attracted a great interest for studying them. Features like the Mott-Insulator–Superfluid transition have been observed [5]. They will also form the basis of the model in the present thesis.

By means of e. g. varying the lattice depth and geometry to tune the tunnelling amplitude and the interaction strength [6], ultracold gases in optical lattices offer great controllability and are used extensively to realize different systems [7]. This idea of simulating quantum-mechanical toy models has gained further traction with the help of Floquet engineering [8]. When driving a static system in a time-periodic fashion, the resulting dynamics of the time-dependent Hamiltonian $\hat{H}(t)$, up to some small scale periodic evolutions, essentially resemble a time-independent effective Hamitonian $\hat{H}_{\mathrm{F}}$ that can in principle be very distinct from the initial system. The form, amplitude and frequency of the driving can be engineered specifically to alter the properties of $\hat{H}_{\mathrm{F}}$. This is exactly the idea we want to harness in this thesis. See [9] for a review on the various effects that have been simulated in this way.

In principle, Floquet engineering can also be used to simulate a model, that inherently exhibits Majorana quasiparticles [10]. Ettore Majorana proposed in 1937 [11], by a reformulation of the relativistic Dirac equation, that there might exist fermions that are their own antiparticles; an attribute that in today's standard model of particle physics is only found with bosons. In recent decades though, physicsts have been trying to find Majorana fermions as quasiparticles in condensed matter systems, where an equal superposition of a particle and a hole can become its own "antiquasiparticle" [12].

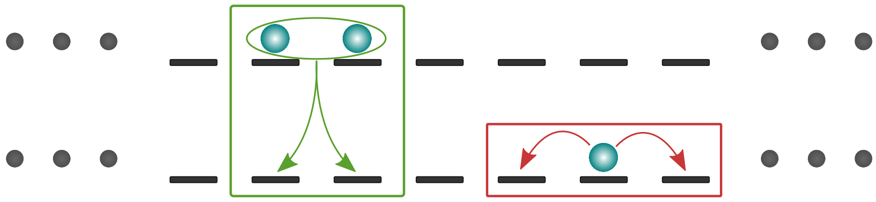

Figure 1.1: Two-leg ladder system. Particles within one leg can move to adjacent sites (red box). The two wires are connected via pair hopping (green box). The model presented in this thesis corresponds to one 2x2 portion like the green box.

Because of their unusual properties, the realization of Majoranas has gained a lot of interest. For instance since they appear as superpositions of fermions at opposite edges of a system, they are highly delocalized which protects them from local pertubations. This makes them an interesting potential platform for low-decoherence quantum computing [13]. They have been proposed theoretically to appear in certain one- and two-dimensional systems connected to superconducting particle reservoirs [12], and first signs of them have been observed experimentally [12, 14].

Recently, there have been proposals for Majorana quasiparticles in a particle-number-conserving setting: a two-leg ladder of lattice sites, see figure 1.1 [15, 16]. Within one leg, particles can move freely. The two legs are connected in a way that particle pairs can tunnel between them, but no single particle can cross the connection. This way, the total particle number as well as the intra-leg parities (even or odd particle number) are conserved and act as protecting symmetries for the Majorana states. The present thesis serves as a preparation for later experimental simulation of this model in an optical lattice. A two-site Hubbard system that features single fermions or pairs on either site will be examined, and a driving potential will be Floquet engineered such that they predominantly tunnel between the sites in pairs. This way, the system corresponds to the inter-leg connection in the two-leg model.

The presentation will be structured as follows:

- Chapter 2 will quickly present the needed background. The Fermi-Hubbard model will be explained and solved exactly for the restricted case of two lattice sites. The theory behind Floquet engineering and its central implications will then be introduced.
- In chapter 3 the theory of Floquet will be applied to the central model of this discourse. The effective Hamiltonian will be computed in the high-driving-frequency limit and compared to a numerical treatment of the system.
- Using the results from the previous chapter, chapter 4 will seek to find parameter sets in which the single-particle tunnelling is suppressed and the pair hopping is enhanced.
- Chapter 5 will conclude the discussion and present an outlook on further steps of the project.

CHAPTER 2

Theoretical Prerequisites

2.1 Fermi-Hubbard Model

Most many-particle systems are at a fundamental level dominated by the interplay of the kinetics of single particles and interactions between them. These interactions can usually be approximated to be of a tight-binding type, i. e. only need to be taken into account for particles below a certain distance apart. This behaviour can be seen for instance in basic models of solids. We picture them as a lattice of atoms, with the outer shell electrons localized at the lattice sites. They interact with other electrons at the same site and can quantum mechanically tunnel to a neighbouring atom. A simple model for these electrons was first proposed in 1963 by John Hubbard [4] and is now known as the Fermi-Hubbard model. In second quantisation language its one dimensional Hamiltonian reads

$$\hat{H} = -J \sum_{i,\sigma} \left(\hat{c}^{\dagger}_{i,\sigma} \hat{c}_{i+1,\sigma} + h.c. \right) + U \sum_{i} \hat{n}_{i,\uparrow} \hat{n}_{i,\downarrow} \,, \tag{2.1}$$

where $\hat{c}^{\dagger}_{i,\sigma}$ and $\hat{c}_{i,\sigma}$ create and annihilate an electron of spin $\sigma \in \{\uparrow, \downarrow\}$ at lattice site i respectively. $\hat{n}_{i,\sigma} = \hat{c}^{\dagger}_{i,\sigma} \hat{c}_{i,\sigma}$ is called the number operator and counts the electrons of spin σ at site i.

Interpreting equation 2.1 is straightforward and depicted in figure 2.1. The first sum runs over all lattice sites i and spins σ and describes the kinetic energy of electrons "hopping" between neighbouring sites i and $i + 1$ with a tunnelling (or hopping) amplitude J[1]. The second term adds an interaction energy U for every on-site pair of electrons.

While the Fermi-Hubbard model was originally proposed to describe electrons in solids, it has proven to be of immense theoretical interest for a wide range of applications and rich physical features. It can be easily generalized to higher-dimensional systems, spin other than $1/2$ or bosonic systems[2]. Other dynamics and interactions can be included in terms of combinations of the creation and annihilation operators $\hat{c}^{\dagger}_{i,\sigma}$ and $\hat{c}_{i,\sigma}$ that can be interpreted in a similar fashion as above.

---

[1] The $h.c.$ in equation 2.1 is standard notation for *hermitian conjugate* and will be used throughout this thesis. I. e. in this case we have $\left(\hat{c}^{\dagger}_{i,\sigma} \hat{c}_{i+1,\sigma}\right)^{\dagger} = \hat{c}^{\dagger}_{i+1,\sigma} \hat{c}_{i,\sigma}$, which mathematically assures the Hamiltonian is hermitian and can be physically interpreted as electrons hopping the other way, from $i + 1$ to i.

[2] It is then known as the Bose-Hubbard model.

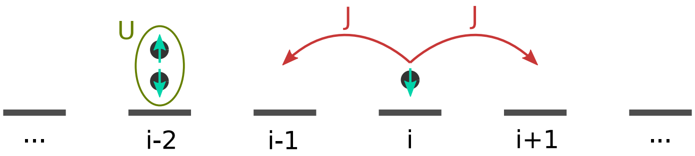

Figure 2.1: 1-dimensional Fermi-Hubbard model for electrons. At each lattice site i either no, one or two electrons with opposite spins can be located. Two electrons at the same site interact due to their spins, yielding an interaction energy U. Electrons can tunnel between neighbouring lattice sites with a hopping amplitude J.

We will now investigate the Fermi-Hubbard model from equation 2.1 to get a grasp of its features. From now on, we will also refer to the particles in this model as fermions, rather than electrons, since it better suits the context of this thesis, in which we ultimately talk about fermionic ultracold gases.

2.1.1 Solving the Hubbard Hamiltonitan

For a given lattice of length L, a suitable Fock basis for the Fermi-Hubbard Hamiltonian from equation 2.1 can be chosen as eigenstates of the number operators $\{\left|n_{1,\uparrow} n_{1,\downarrow} \cdots n_{L,\uparrow} n_{L,\downarrow}\right\rangle\}$ obeying

$$\hat{n}_{i,\sigma} \left|n_{1,\uparrow} n_{1,\downarrow} \cdots n_{L,\uparrow} n_{L,\downarrow}\right\rangle = n_{i,\sigma} \left|n_{1,\uparrow} n_{1,\downarrow} \cdots n_{L,\uparrow} n_{L,\downarrow}\right\rangle \ .$$

The total number of fermions N given by acting with the total number operator $\hat{N} = \sum_{i=1}^{L}(\hat{n}_{i,\uparrow} + \hat{n}_{i,\downarrow})$ on the states remains constant in time, since $[\hat{N}, \hat{H}] = 0$. Similarly $[\hat{M}, \hat{H}] = 0$ for the total magnetization operator $\hat{M} = \frac{1}{2}\sum_{i=1}^{L}(\hat{n}_{i,\uparrow} - \hat{n}_{i,\downarrow})$. Hence, we can always separate the full Hilbert space $\mathcal{H} = \oplus_{N,M}\mathcal{H}^{(N,M)}$ into subspaces $\mathcal{H}^{(N,M)}$ of equal fermion number N and total magnetization M.

The Two Site Hubbard Model at Zero Temperature

Consider the case of a two-site Fermi-Hubbard model at half-filling for opposite spin fermions, i. e. $L = N = 2$ and $M = 0$, at absolute zero. The system will thus be in the ground state, which we will compute now. In $\mathcal{H}^{(2,0)}$, spanned by $\{|1001\rangle, |1100\rangle, |0110\rangle, |0011\rangle\}$, $\hat{H}$ can be written down as

$$\hat{H} \doteq \begin{pmatrix} 0 & -J & 0 & -J \\ -J & U & J & 0 \\ 0 & J & 0 & J \\ -J & 0 & J & U \end{pmatrix},$$

where " $\doteq$ " ist meant to be read as "is represented by". We denote the set of eigenstates of $\hat{H}$ by $\{|(N,M);i\rangle\}_i$ with energies $E_i^{(N,M)}$. Up to proper normalization, they are given by

$$\begin{pmatrix} |(2,0);1\rangle \\ |(2,0);2\rangle \\ |(2,0);3\rangle \\ |(2,0);4\rangle \end{pmatrix} = \begin{pmatrix} 1 & 0 & 1 & 0 \\ 0 & -1 & 0 & 1 \\ e_+ & 1 & -e_+ & 1 \\ e_- & 1 & -e_- & 1 \end{pmatrix} \cdot \begin{pmatrix} |1001\rangle \\ |1100\rangle \\ |0110\rangle \\ |0011\rangle \end{pmatrix}, \tag{2.2}$$

$$\text{where} \quad e_\pm = \frac{1}{4}\left(U/J \pm \operatorname{sign}(J)\sqrt{16 + (U/J)^2}\right)$$

with corresponding energies $E_1^{(2,0)} = 0$, $E_2^{(2,0)} = U$, $E_3^{(2,0)} = 2Je_-$ and $E_4^{(2,0)} = 2Je_+$. Thus we see, that for any J and U, the ground state is given by $|(2,0);3\rangle$. To examine the features of the system, we will now look at some notable observables. By using the expression for $|(2,0);3\rangle$ in eq. 2.2 and reintroducing the normalization, we find that the total kinetic energy[3] of the ground state is given by

$$\langle\sum_\sigma\left(\hat{c}^\dagger_{1,\sigma}\hat{c}_{2,\sigma} + h.c.\right)\rangle_{\mathrm{GS}} = \langle(2,0);3|\sum_\sigma\left(\hat{c}^\dagger_{1,\sigma}\hat{c}_{2,\sigma} + h.c.\right)|(2,0);3\rangle = \frac{4e_+}{1+e_+^2}\,, \tag{2.3}$$

where we remind ourselves to interpret the operator $\hat{c}^\dagger_{i,\sigma}\hat{c}_{j,\sigma}$ as a fermion hopping from site j to site i. Similarly, we find pairs of fermions hopping together as

$$\langle\hat{c}^\dagger_{1,\uparrow}\hat{c}^\dagger_{1,\downarrow}\hat{c}_{2,\downarrow}\hat{c}_{2,\uparrow} + h.c.\rangle_{\mathrm{GS}} = \frac{1}{1+e_+^2}\,, \tag{2.4}$$

and the total average amount of on-site pairs $\hat{N}_{\mathrm{pair}} = \sum_{i=1}^2 \hat{n}_{i,\uparrow}\hat{n}_{i,\downarrow}$ as

$$\langle\hat{N}_{\mathrm{pair}}\rangle_{\mathrm{GS}} = \frac{1}{1+e_+^2}\,. \tag{2.5}$$

They are visualized in figure 2.2.

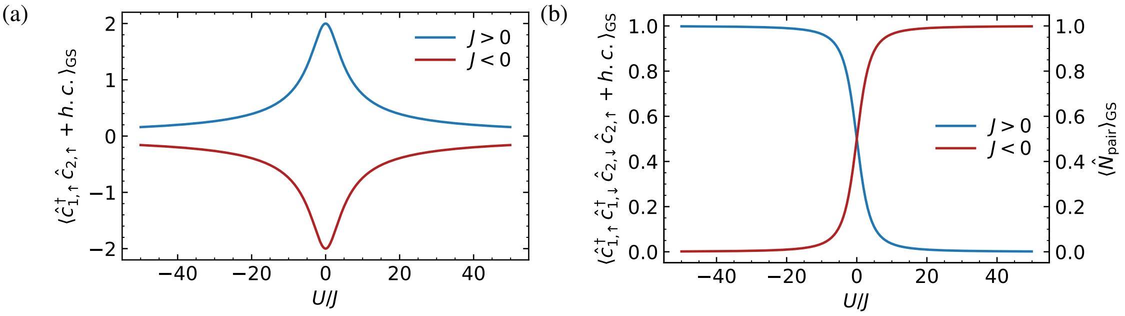

Figure 2.2: (a) Kinetic energy of the ground state $|(2,0);3\rangle$, (b) average pair hopping and on-site pairs.

There are three distinct regions. Assuming positive J:

1. For $U/J = 0$, there is no interaction, and the fermions can move freely between the two sites, leading to a high kinetic energy. Since it does not make any difference in energy, whether the fermions pair up or not, we statistically find pairs about half of the times.

2. For $U/J \ll 0$, i. e. for $U < 0$, it is favourable for the fermions to pair up, since it lowers the total energy. Hence, the fermions are likely to hop in pairs (figure 2.2(b)), but there is only a low probability for the fermions to move alone (figure 2.2(a)).

3. In the opposite limit of $U/J \gg 0$, the fermions repel each other, ultimately freezing all motion.

We can think of the case $U/J \gg 0$ as a very basic demonstration of a Mott insulator, in which the conductivity of a material drops to zero because the strong repulsion of the charge carriers freezes the

---

[3] up to the correct energy scale

system. $U/J \ll 0$ refers to the so-called superfluid effect. In the regions of low $|U/J|$, we see some transitional state between the two limiting cases. To be more genuine, we would have to look at longer chains with more fermions and the interested reader is directed to [17] for a more elaborate discussion. Yet some of the consequences of the interplay between kinetic and interaction energy in the Hubbard model can be seen even in this very low-dimensional case.

Out of Equilibrium

To introduce an important concept of this thesis, we will stay in the two-site model but move on from the static ground state of the system and consider a single fermion. Without loss of generality, we choose it to be of type spin up and to lie at site $j = 1$ at time $t_0 = 0$. In $\mathcal{H}^{(1,+1/2)}$ a suitable basis can be chosen as $\{|1000\rangle, |0010\rangle\}$, corresponding to a fermion with spin up at either of the two sites. In this basis $\big|\psi(t_0 = 0)\big\rangle = |1000\rangle$ and the Fermi-Hubbard-Hamiltonian from equation 2.1 is given by

$$\hat{H}\big|_{\mathcal{H}^{(1,+1/2)}} \doteq \begin{pmatrix} 0 & -J \\ -J & 0 \end{pmatrix} . \tag{2.6}$$

Since the Hamiltonian is time independent, the evolved state $|\psi(t)\rangle$ at time t is simply given by

$$|\psi(t)\rangle = \hat{U}(t,0)\big|\psi(t_0 = 0)\big\rangle = \hat{U}(t,0)\,|1000\rangle$$

where the time evolution operator $\hat{U}(t,t_0) = \exp\!\Big(-i\frac{\hat{H}}{\hbar}(t-t_0)\Big)$ obeys

$$\begin{aligned}\hat{U}(t,t_0) &\doteq \exp\left[-i\frac{t-t_0}{\hbar}\begin{pmatrix} 0 & -J \\ -J & 0 \end{pmatrix}\right] = \sum_{n=0}^{\infty}\frac{1}{n!}\left(\frac{i(t-t_0)J}{\hbar}\right)^n \underbrace{\begin{pmatrix} 0 & 1 \\ 1 & 0 \end{pmatrix}^n}_{=\mathbb{1}\text{ for n even.}} \\ &= \cos\!\left(\frac{J}{\hbar}(t-t_0)\right)\mathbb{1} + i\sin\!\left(\frac{J}{\hbar}(t-t_0)\right)\begin{pmatrix} 0 & 1 \\ 1 & 0 \end{pmatrix} .\end{aligned}$$

With this, we readily obtain

$$|\psi(t)\rangle = \cos\!\left(\frac{tJ}{\hbar}\right)|1000\rangle + i\sin\!\left(\frac{tJ}{\hbar}\right)|0010\rangle .$$

What we have found is that the particle oscillates back and forth between the two sites with a frequency of $\Omega = 2\frac{J}{\hbar}$. To make the factor 2 more apparent, one can look at the occupation densities, i. e.

$$\begin{aligned}\langle\hat{n}_{1,\uparrow}\rangle(t) &= \langle\psi(t)|\,\hat{n}_{1,\uparrow}\,|\psi(t)\rangle = \cos\!\left(\frac{2J}{\hbar}\right)^2 = \frac{1}{2}\left[1 + \cos\!\left(\frac{2J}{\hbar}t\right)\right] \\ \langle\hat{n}_{2,\uparrow}\rangle(t) &= \frac{1}{2}\left[1 - \cos\!\left(\frac{2J}{\hbar}t\right)\right] .\end{aligned} \tag{2.7}$$

Notice, that the frequency Ω at which the densities oscillate is directly proportional to the hopping amplitude J. We will later deal with a more complicated Hamiltonian, but find that it approximately behaves just like the Hubbard Hamiltonian from equation 2.1 with some effective hopping amplitude J_{eff}. The proportionality will turn out to be very useful, since we can deduce the size of J_{eff} reversely by calculating Ω numerically.

2.2 Floquet Theory

In essence, Floquet Theory tells us that the time evolution generated by a time periodic Hamiltonian $\hat{H}(t) = \hat{H}(t+T)$ will up to small scale periodic dynamics ultimately be governed by a time-independent effective Hamiltonian $\hat{H}_\mathrm{F}$. If one adds a time periodic driving to some static model, $\hat{H}_\mathrm{F}$ can in principle attain attributes very distinct from the initial model. Floquet engineering aims to design the driving such that $\hat{H}_\mathrm{F}$ contains some desired features.

To introduce the theory behind it, we will first remind ourselves on Bloch's theorem for spatially periodic potentials in section 2.2.1. Arguing, that Bloch's theorem is only one example of a more general mathematical theorem on periodic differential equations, we will see that something similar exists for time periodicity, which will be introduced as Floquet's theorem in section 2.2.2. After some notes on its implications in section 2.2.3, we will end this discussion with a perturbative approach to find $\hat{H}_\mathrm{F}$ in 2.2.4.

2.2.1 Revision: Bloch's Theorem for Spatially-Periodic Potentials

Recall, that for a one-dimensional[4] spatially periodic potential $V(x) = V(x+L)$, e. g. for electrons in the periodic potential well of atoms in a solid lattice, the solutions to the time independent Schrödinger equation $\hat{H}(x)\psi_n(x) = E_n\psi_n(x)$ can be written as plane waves times a periodic function $u_n(x) = u_n(x+L)$ like

$$\psi_n(x) = \mathrm{e}^{-ik_n x} u_n(x) \, , \tag{2.8}$$

where k_n is called the *quasi-* or *crystal-momentum* of the state ψ_n. This is known as Bloch's theorem and the wave functions $\psi_n(x)$ are called *Bloch waves*. It follows from its derivation that the k_n are only defined up to integer multiples of $2\pi/L$, k_n and $k_n + 2\pi/L$ describe the same Bloch wave $\psi_n(x)$. By convention, k_n is nearly always chosen to lie in the first *Brioullin zone*, i. e. the first intervall of $2\pi/L$.

Bloch's theorem is of great importance in solid state physics since the quasimomenta lead to the band model of solids and thus in particular to our understanding of electrical conductance. It was first formulated for the problem of electrons in a solid by Felix Bloch in 1929 [18]. For a more in depth discussion and a derivation of the theorem the reader is directed to chapter 8 of [19].

In fact, Bloch's theorem is just one example to an underlying mathematical theorem for periodic differential equations, found by Gaston Floquet in 1883 [20], and essentially states, that the solutions to periodic differential equations can be written as some phase multiplied by a periodic function (cf. eq. 2.8). Thus, we can derive closely related results for the time dependent Schrödinger equation with time-periodic potentials, which we will now move on to.

2.2.2 Time-Periodic Potentials

Let $\hat{V}(t) = \hat{V}(t+T)$ be a time-periodic potential. The full Hamiltonian $\hat{H}(t)$, and with it the time-dependent Schrödinger equation

$$i\hbar \frac{\mathrm{d}}{\mathrm{d}t} \left|\psi(t)\right\rangle = \hat{H}(t) \left|\psi(t)\right\rangle \, , \tag{2.9}$$

---

[4] We restrict ourselves to the one-dimensional case for simplicity. The theorem works analogously in higher dimensions.

are thus also T-periodic, i. e. periodic with period T, and hence Floquet's theorem applies. In analogy to how the spatially-periodic equation in the previous section lead to the solutions being Bloch waves, the solutions $|\psi(t)\rangle$ of equation 2.9, can be decomposed in terms of the so called *Floquet states*

$$\left|\psi_n(t)\right\rangle = \mathrm{e}^{-i\epsilon_n t/\hbar}\left|u_n(t)\right\rangle \,, \tag{2.10}$$

where $\left|u_n(t)\right\rangle = \left|u_n(t+T)\right\rangle$ denote time-periodic *Floquet modes* with corresponding *quasienergies* ϵ_n. Notice the perfect analogy to the Bloch waves in equation 2.8. We could stop here without further proof by referring to Floquet's theorem, but to gain a better understanding of this Floquet picture we will introduce it in a different fashion, roughly following [8] and [21]. The time evolution operator $\hat{U}(t+T,t)$ over one period T will play an important role here[5]. Thus, we will first need to have a look at what the periodicity of $\hat{H}(t)$ implies on the operator $\hat{U}(t,t_0)$ before we can move on to find the Floquet states and prove equation 2.10.

The time-evolution operator $\hat{U}(t,t_0)$ by definition is unitary and obeys the composition property $\hat{U}(t,t_0) = \hat{U}(t,t')\hat{U}(t',t_0)$, the initial condition $\hat{U}(t_0,t_0) = \mathbb{1}$, and the Schrödinger-like equation

$$i\hbar\frac{\mathrm{d}}{\mathrm{d}t}\hat{U}(t,t_0) = \hat{H}(t)\hat{U}(t,t_0)\,. \tag{2.11}$$

Since

$$\begin{aligned}
i\hbar\frac{\mathrm{d}}{\mathrm{d}t}\hat{U}(t+T,t_0+T) &= \left(i\hbar\frac{\mathrm{d}}{\mathrm{d}t}\hat{U}(t+T,t_0)\right)\hat{U}(t_0,T)\\
&= \left(i\hbar\frac{\mathrm{d}}{\mathrm{d}(t+T)}\hat{U}(t+T,t_0)\right)\hat{U}(t_0,T)\\
&= \hat{H}(t+T)\hat{U}(t+T,t_0)\hat{U}(t_0,T)\\
&= \hat{H}(t)\hat{U}(t+T,t_0+T)\,,
\end{aligned}$$

and $\hat{U}(t_0+T,t_0+T) = \mathbb{1}$, the operator $\hat{U}(t+T,t_0+T)$ obeys the same differential equation as $\hat{U}(t,t_0)$ while fulfilling the same initial condition. Hence the periodicity of $\hat{H}(t)$ implies that

$$\hat{U}(t+T,t_0+T) = \hat{U}(t,t_0)\,. \tag{2.12}$$

Now define the eigenstates $\left|\psi_n(t)\right\rangle$ of the full-period time-evolution operator $\hat{U}(t+T,t)$ at time t to corresponding eigenvalue $a_n(t)$ as

$$\hat{U}(t+T,t)\left|\psi_n(t)\right\rangle = a_n(t)\left|\psi_n(t)\right\rangle\,.$$

These $\left|\psi_n(t)\right\rangle$ are solutions to the Schrödinger equation 2.9. To see this, consider $\hat{U}(t,t_0)\left|\psi_n(t_0)\right\rangle$. It

---

[5] Similar to the translation operator $\hat{T}_{\mathbf{L}}$ over one lattice vector $\mathbf{L}$ in the derivation of Bloch's theorem (cf. the first proof of Bloch's theorem in chapter 8 in [19]).

is easy to see by equation 2.11 that this state obeys the Schrödinger equation. Also

$$\begin{aligned}\hat{U}(t+T,t)\cdot\hat{U}(t,t_0)\left|\psi_n(t_0)\right\rangle &= \underbrace{\hat{U}(t+T,t)\hat{U}(t,t_0)\hat{U}(t_0,t_0+T)}_{\hat{U}(t+T,t_0+T)\overset{2.12}{=}\hat{U}(t,t_0)}\underbrace{\hat{U}(t_0+T,t_0)\left|\psi_n(t_0)\right\rangle}_{a_n(t_0)\left|\psi_n(t_0)\right\rangle}\\ &= a_n(t_0)\cdot\hat{U}(t,t_0)\left|\psi_n(t_0)\right\rangle\ ,\end{aligned}$$

where we have inserted $\hat{\mathbb{1}}=\hat{U}(t_0,t_0+T)\hat{U}(t_0+T,t_0)$ in the first line. Thus, the state $\hat{U}(t,t_0)\left|\psi_n(t_0)\right\rangle$ is an eigenstate of $\hat{U}(t+T,t)$ and can be identified with $\left|\psi_n(t)\right\rangle$. Hence, the states $\left|\psi_n(t)\right\rangle$ obey the Schrödinger equation. Note that this also proves that the eigenvalues $a_n(t_0)=a_n(t)\equiv a_n$ are independent of t.

We now know that the eigenstates $\left|\psi_n(t)\right\rangle$ of the full-period time-evolution operator $\hat{U}(t+T,t)$ with corresponding eigenvalues a_n are solutions to the time-dependent Schrödinger equation. It remains to show that they have the form of the Floquet states form equation 2.10. By definition

$$\left|\psi_n(t+T)\right\rangle=\hat{U}(t+T,t)\left|\psi_n(t)\right\rangle=\underbrace{\mathrm{e}^{-i\epsilon_nT/\hbar}}_{a_n}\left|\psi_n(t)\right\rangle\ , \tag{2.13}$$

where we used the unitarity of $\hat{U}(t+T,t)$ in the last equality to write its eigenvalues as a phase factor. We can now formally construct the functions $\left|u_n(t)\right\rangle=\mathrm{e}^{i\epsilon_nt/\hbar}\left|\psi_n(t)\right\rangle$, which by use of equation 2.13 can be seen to be periodic, i. e. $\left|u_n(t+T)\right\rangle=\left|u_n(t)\right\rangle$. With these we can decompose $\left|\psi_n(t)\right\rangle$ as

$$\left|\psi_n(t)\right\rangle=\mathrm{e}^{-i\epsilon_nt/\hbar}\left|u_n(t)\right\rangle\ .$$

We have thus proven equation 2.10. The eigenstates $\left|\psi_n(t)\right\rangle$ of the full period time evolution operator $\hat{U}(t+T,t)$ can be identified with the Floquet states and their eigenvalues $a_n=\mathrm{e}^{-i\epsilon_nT/\hbar}$ define the quasienergies ϵ_n.

2.2.3 Implications of the Floquet States

Equation 2.10 has some very interesting implications for the study of time-periodic systems. To find the first one, we extract the time evolution from equation 2.10. We can write[6]

$$\hat{U}(t,t_0)=\hat{U}_{\mathrm{M}}(t,t_0)\exp\Big(-i(t-t_0)\hat{H}^{\mathrm{F}}_{t_0}/\hbar\Big)\,, \tag{2.14}$$

where $\hat{U}_{\mathrm{M}}(t,t_0)$ describes the small-scale periodic time evolution of the Floquet modes, the *micromotion*,

$$\hat{U}_{\mathrm{M}}(t,t_0)\left|u_n(t_0)\right\rangle=\left|u_n(t)\right\rangle\ ,$$

and $\hat{H}^{\mathrm{F}}_{t_0}$ is diagonalized by the Floquet modes $\left|u_n(t_0)\right\rangle$ at t_0 with eigenvalues ϵ_n[7].

---

[6] We could have derived the Floquet states by directly constructing this time-evolution operator for a periodic Hamiltonian and then propagating an arbitrary state in time (see [21]).

[7] The reader is asked to confirm that $\hat{U}(t,t_0)$ from eq. 2.14 acting on $\left|\psi(t_0)\right\rangle=\sum_n\mathrm{e}^{-i\epsilon_nt_0/\hbar}\left|u_n(t_0)\right\rangle$ yields the correctly propagated state $|\psi(t)\rangle$.

Looking at equation 2.14, we can see that $\hat{H}^{\mathrm{F}}_{t_0}$ generates the time-evolution operator over one period as $\exp\left(-i\hat{H}^{\mathrm{F}}_{t_0}T/\hbar\right) = \hat{U}(t_0+T, t_0)$. In this very sense, we can interpret $\hat{H}^{\mathrm{F}}_{t_0}$ as follows: It seems like the system is simply governed by this time-independent Hamiltonian if we only look at the time evolution in stroboscopic steps of T. We call $\hat{H}^{\mathrm{F}}_{t_0}$ the *Floquet Hamiltonian* and its eigenvalues ϵ_n quasienergies, since they determine the stroboscopic time evolution in much the same way the energy eigenvalues do in a time-independent system. We can picture the interplay of periodic micromotion and the large scale phase of equation 2.14 visually like a sine wave on top of another function. To summarise:

> The time evolution described by a time periodic Hamiltonian $\hat{H}(t) = \hat{H}(t+T)$ can be separated into a small scale, T-periodic micromotion and a large scale phase factor. In a stroboscopic sense the dynamics are determined by a time-independent Floquet Hamiltonian $\hat{H}^{\mathrm{F}}_{t_0}$ in steps of T.

It was already notationally implied that while $\hat{H}^{\mathrm{F}}_{t_0}$ is time independent, it is defined for an initial time t_0. For some other t_0' it can be constructed via $\hat{H}^{\mathrm{F}}_{t_0'} = \hat{U}^\dagger(t, t_0')\hat{H}^{\mathrm{F}}_{t_0}\hat{U}(t, t_0')$, as can be seen from equation 2.14. Since this initial time is chosen arbitrarily, we would like to have some other, more symmetric way of describing the system. There is a different approach to Floquet theory (cf. [9]) that rather than relying on the analogy to Bloch's theorem, starts by formally constructing a gauge transformation

$$\hat{H}_{\mathrm{F}} = \hat{U}^\dagger_{\mathrm{F}}(t)\hat{H}(t)\hat{U}_{\mathrm{F}}(t) - i\hbar\hat{U}^\dagger_{\mathrm{F}}(t)\dot{\hat{U}}_{\mathrm{F}}(t) \tag{2.15}$$

of the Hamiltonian $\hat{H}(t)$ with a T-periodic unitary operator $\hat{U}_{\mathrm{F}}(t) = \hat{U}_{\mathrm{F}}(t+T)$ in such a way that $\hat{H}_{\mathrm{F}}$, describing the evolution of a state $|\psi_{\mathrm{F}}(t)\rangle = \hat{U}^\dagger_{\mathrm{F}}(t)\,|\psi(t)\rangle$[8], is time independent. This $\hat{H}_{\mathrm{F}}$ is called the *effective Hamiltonian*. The evolution of $|\psi(t)\rangle$ can then be determined by first transforming into the gauge system with $\hat{U}^\dagger_{\mathrm{F}}(t)$, then propagating the state in this gauge with $\hat{H}_{\mathrm{F}}$ and finally transforming back into the original system with $\hat{U}_{\mathrm{F}}(t)$, i. e.

$$\hat{U}(t, t_0) = \hat{U}_{\mathrm{F}}(t)\exp(-i(t-t_0)\hat{H}_{\mathrm{F}}/\hbar)\hat{U}^\dagger_{\mathrm{F}}(t_0)\,. \tag{2.16}$$

Comparing this to equation 2.14, the effective Hamiltonian determines the time evolution in a similar manner to $\hat{H}^{\mathrm{F}}_{t_0}$, while staying independent of the initial phase t_0. To see how exactly the two approaches are connected, note that the choice of the gauge, and with it the effective Hamiltonian, are not unique. Specifically we could insert a $\mathbb{1} = \hat{U}^\dagger_{\mathrm{F}}(t_0)\hat{U}_{\mathrm{F}}(t_0)$ to the left of the exponential in equation 2.16 to attain

$$\hat{U}(t, t_0) = \hat{U}_{\mathrm{F}}(t)\hat{U}^\dagger_{\mathrm{F}}(t_0)\exp\left(-i(t-t_0)\hat{U}_{\mathrm{F}}(t_0)\hat{H}_{\mathrm{F}}\hat{U}^\dagger_{\mathrm{F}}(t_0)/\hbar\right),$$

which would be equivalent to choosing another gauge $\hat{U}'_{\mathrm{F}}(t) = \hat{U}_{\mathrm{F}}(t)\hat{U}^\dagger_{\mathrm{F}}(t_0)$ that fulfils $\hat{U}'_{\mathrm{F}}(t_0) = \mathbb{1}$ and $\hat{H}'_{\mathrm{F}} = \hat{U}_{\mathrm{F}}(t_0)\hat{H}_{\mathrm{F}}\hat{U}^\dagger_{\mathrm{F}}(t_0)$. Comparing this to equation 2.14, we can identify

$$\begin{aligned} \hat{H}^{\mathrm{F}}_{t_0} &= \hat{H}'_{\mathrm{F}} = \hat{U}_{\mathrm{F}}(t_0)\hat{H}_{\mathrm{F}}\hat{U}^\dagger_{\mathrm{F}}(t_0) \qquad \text{and} \\ \hat{U}_{\mathrm{M}}(t, t_0) &= \hat{U}'_{\mathrm{F}}(t) = \hat{U}_{\mathrm{F}}(t)\hat{U}^\dagger_{\mathrm{F}}(t_0)\,. \end{aligned}$$

---

[8] The form of eq. 2.15 follows from demanding that $i\hbar\,\mathrm{d}_t\,|\psi_{\mathrm{F}}(t)\rangle = \hat{H}_{\mathrm{F}}\,|\psi_{\mathrm{F}}(t)\rangle$.

In the general arbitrary gauge, $\hat{H}_{\mathrm{F}}$ and $\hat{H}^{\mathrm{F}}_{t_0}$ are thus related by a unitary transformation. The gauge can however be chosen in such a way, that they coincide. Also, the gauge transformation $\hat{U}_{\mathrm{F}}(t)$ describes the micromotion. From now on we will thus refer to $\hat{U}_{\mathrm{F}}(t)$ as the micromotion operator. We see:

> The time-independent effective Hamiltonian $\hat{H}_{\mathrm{F}}$ provides a similar insight into the dynamics like $\hat{H}^{\mathrm{F}}_{t_0}$, while being independent of the initial time t_0. It generates the same quasienergy spectrum as $\hat{H}^{\mathrm{F}}_{t_0}$, since they are related by a unitary transformation.

Again, in close analogy to the quasimomenta in Bloch's theorem, the quasienergies ϵ_n are only defined up to some integer multiple of $\hbar\omega$, where $\omega = 2\pi/T$, since they were introduced as the phases of the eigenvalues $\mathrm{e}^{-i\epsilon_n T/\hbar}$ of the full-period time-evolution operator $\hat{U}(t+T,t)$ and $\epsilon_{nm} = \epsilon_n + m\hbar\omega$ does not change these values for $m \in \mathbb{Z}$. Since the eigenstates of $\hat{U}(t+T,t)$, namely the Floquet states, have to be unique, we can find new Floquet modes $|u_{nm}(t)\rangle = |u_n(t)\rangle\, \mathrm{e}^{im\omega t}$, such that

$$|\psi_n(t)\rangle = \mathrm{e}^{-i\epsilon_{nm}t/\hbar}\,|u_{nm}(t)\rangle = \mathrm{e}^{-i\epsilon_n t/\hbar}\,|u_n(t)\rangle\ . \tag{2.17}$$

With the quasienergies as its defining eigenvalues, this also implies that $\hat{H}^{\mathrm{F}}_{t_0}$ is not unique. Choosing a set of ϵ_n is arbitrary. In analogy to Bloch's theorem, it is often customary to define them all to lie within one *Brioullin zone* of $\hbar\omega$, but sometime it is useful to make a different choice [21]. One way around this is to plug equation 2.17 into the Schrödinger equation, which after using the product rule yields

$$\left(\hat{H}(t) - i\hbar\,\mathrm{d}_t\right)|u_{nm}(t)\rangle = \epsilon_{nm}\,|u_{nm}(t)\rangle\ .$$

We can interpret this as an eigenvalue equation for the quasienergy operator $\hat{Q} = \hat{H}(t) - i\hbar\mathrm{d}_t$ in an extended Hilbert space. Diagonalization of this operator yields the full quasienergy spectrum. For the sake of this thesis this is not of high importance, so this should suffice as an entry point into other literature. For an in depth discussion see [8] or [21]. The important takeaway is:

> The quasienergies ϵ_n are only defined up to multiples of $\hbar\omega$, where $\omega = 2\pi/T$. The generalised quasienergies $\epsilon_{nm} = \epsilon_n + m\hbar\omega$, $m \in \mathbb{Z}$, correspond to the same Floquet states $|\psi_n(t)\rangle$.

At this point, all the necessary theory for the idea of Floquet engineering has been introduced. The described implications allow us to attain the long-term dynamics of the time-dependent Schrödinger equation, without the need to know all the details happening within one driving period. The effective (or the Floquet) Hamiltonian generates these long-term dynamics. The goal is to engineer the parameters of the original Hamiltonian in such a way, that $\hat{H}_{\mathrm{F}}$ describes a system with desired properties.

Before we move on to how we can systematically find the effective Hamiltonian, one last note is needed. The theory of Floquet states can be generalized to Hamiltonians that are only time-periodic up to slow parameter variations, i. e. for slow, adiabatic turning on of some periodic driving. This will be important for section 3.2.1. A full discussion of the theoretic derivations will not fit into the scope of this thesis and will be therefore be left out[9]. The interested reader is directed to [22].

---

[9] It essentially comes down to treating time as a coordinate in the above-mentioned extended Hilbert space and introducing a new artificial time describing the slow variations.

2.2.4 The Effective Description for High Driving Frequencies

For a general time-periodic Hamiltonian $\hat{H}(t)$ there is no easy way to find an exact form for $\hat{H}_\mathrm{F}$. There are notable and instructive exceptions to this, see e. g. [21] for a discussion on a two level system in a circularly polarized classical radiation field, where the gauge transformation $\hat{U}_\mathrm{F}(t)$ is simply a transformation into the rotating frame of reference, or the treatement of the linearly forced harmonic oscillator in [23]. For systems in which we cannot intuitively guess the gauge transformation, we have to rely on perturbative approaches. Both $\hat{U}_\mathrm{F}(t)$ and the effective Hamiltonian $\hat{H}_\mathrm{F}$ can be expanded in orders of the inverse driving frequency. In this thesis, we will only be interested in the expansion for $\hat{H}_\mathrm{F}$. Since $\hat{H}(t)$ is T-periodic, we can write its Fourier components as

$$\hat{H}_m = \frac{1}{T}\int_0^T \mathrm{d}t \hat{H}(t) \mathrm{e}^{-im\omega t} \,.$$

To n-th order, the effective Hamiltonian is expanded as $\hat{H}_\mathrm{F}^{[n]} = \sum_{k=1}^{n} \hat{H}_\mathrm{F}^{(k)}$. The leading order terms are given by (cf. [8])

$$\begin{aligned}
\hat{H}_\mathrm{F}^{(1)} &= \hat{H}_0 \,, \\
\hat{H}_\mathrm{F}^{(2)} &= \sum_{m=1}^{\infty} \frac{\left[\hat{H}_m, \hat{H}_{-m}\right]}{m\hbar\omega} \,, \\
\hat{H}_\mathrm{F}^{(3)} &= \sum_{m\neq 0} \left(\frac{\left[\hat{H}_{-m}, \left[\hat{H}_0, \hat{H}_m\right]\right]}{2(m\hbar\omega)^2} + \sum_{m'\neq 0,m} \frac{\left[\hat{H}_{-m'}, \left[\hat{H}_{m'-m}, \hat{H}_m\right]\right]}{3mm'(\hbar\omega)^2} \right) .
\end{aligned}$$

One way to derive these is to block diagonalize the before-mentioned quasienergy operator. This is equivalent to finding a time-independent gauge-transformed Hamiltonian and thus the effective Hamiltonian (cf. eq. 2.15) which is the ansatz chosen in [8]. For a different but equivalent approach, see [24]. As an interesting remark, notice that to leading order the effective Hamiltonian is simply given by the time-averaged Hamiltonian $\hat{H}_0$. This fulfils our classical intuition, that for very large frequency a time periodic driving the inertial system only “senses” the average driving.

CHAPTER 3

Driving the Two-Site Hubbard Model

We will now revisit the two-site Fermi-Hubbard Hamiltonian from section 2.1.1, which we will refer to as the static model $\hat{H}_\mathrm{S}$ from now on. We remind ourselves that (cf. eq. 2.1)

$$\hat{H}_\mathrm{S} = -J \sum_{\sigma} \left(\hat{c}^{\dagger}_{1,\sigma} \hat{c}_{2,\sigma} + h.c. \right) + U \left(\hat{n}_{1,\uparrow} \hat{n}_{1,\downarrow} + \hat{n}_{2,\uparrow} \hat{n}_{2,\downarrow} \right) . \tag{3.1}$$

Using the techniques outlined in section 2.2, we want to alter the effective properties of the model by introducing an additional T-periodic driving potential

$$\hat{V}(t) = \frac{\kappa}{2} \sin \omega t \sum_{\sigma} \left(-\hat{n}_{1,\sigma} + \hat{n}_{2,\sigma} \right) ,$$

where κ denotes the amplitude and ω the frequency of the driving. The full, driven two-site model in question is then given by

$$\hat{H}(t) = \hat{H}_\mathrm{S} + \hat{V}(t) . \tag{3.2}$$

Floquet's theorem tells us that this new Hamiltonian is essentially describing the dynamics of some independent effective Hamiltonian $\hat{H}_\mathrm{F}$. In this chapter, we want to study this effective description.

After a first numerical look at the dynamics generated by equation 3.2 in section 3.1, $\hat{H}_\mathrm{F}$ will be calculated in the high-driving-frequency limit in section 3.2. We will then compare the two approaches in 3.2.1 and 3.2.2, verify the validity of the approximation and study where it breaks down.

3.1 Numerical Solution

For small enough time steps dt a general time-dependent Hamiltonian $\hat{H}(t)$ can be assumed to be constant and the time evolution from t_0 to $t_0 + dt$ can be approximated by the unitary operator

$$\hat{U}(t_0 + dt, t_0) \approx \exp\left(i \frac{\hat{H}(t_0)}{\hbar} dt \right) ,$$

such that when starting with a state $\left| \psi(t_0) \right\rangle$, the time-evolved state $\left| \psi(t_0 + dt) \right\rangle$ can be written as

$$\left| \psi(t_0 + dt) \right\rangle = \hat{U}(t_0 + dt, t_0) \left| \psi(t_0) \right\rangle \approx \exp\left(i \frac{\hat{H}(t_0)}{\hbar} dt \right) \left| \psi(t_0) \right\rangle . \tag{3.3}$$

One can then in principle approximately compute the state $|\psi(t)\rangle$ at any time t by applying this procedure repeatedly. In practice, equation 3.3 is realized in the chosen reduced Hilbert space $\mathcal{H}^{(N,M)}$ with the representations of the vector $|\psi(t_0)\rangle$ and the matrix operator $\hat{U}(t_0+dt,t_0)$ in the given basis. The exponential can be computed by first changing into the numerically calculated eigenbasis of $\hat{H}(t_0)$, then evolving the state by exponentiating the diagonal form of $\hat{H}(t_0)$ and finally changing into the old basis again. For matrix representations of our driven model equation 3.2 see appendix A.

A sample evolution of the Hamiltonian from equation A.1, is pictured in figure 3.1, where the system started with a pair of two fermions at site $j = 1$. The time evolution of the state is visualized by the dynamics of this pair. It fulfils our basic intuition, that the pair hopping is roughly connected to the rate of change of pairs. Also, if we neglect small scale oscillations, the pairs simply oscillate between the two sites. This is already a sign of the underlying effective model.

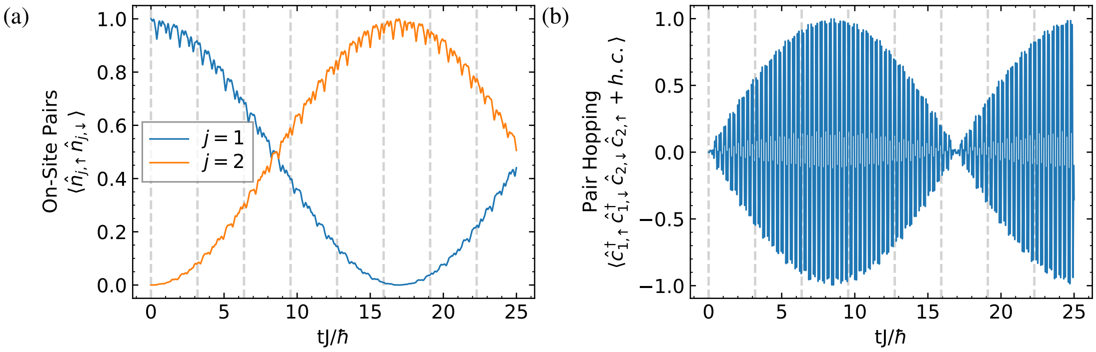

Figure 3.1: A sample time evolution of $\hat{H}(t)$, starting with two fermions at site $j = 1$. The evolution of the the pair is shown by (a) its location and (b) the pair hopping $\langle \hat{c}^\dagger_{1,\uparrow}\hat{c}^\dagger_{1,\downarrow}\hat{c}_{2,\downarrow}\hat{c}_{2,\uparrow} + h.c.\rangle$. The gray vertical lines indicate full periods $2\pi/\omega$ of the driving. Here, $U/J = -8$, $\kappa/\hbar\omega = 1.5$ and $\hbar\omega/J = 20$.

Choosing the Time Step dt

It is important to choose the time step dt small enough such that the numerics are well converged. This problem is demonstrated in figure 3.2(a). It shows the numerical evolution for a single fermion starting at site $j = 1$. The dynamics change considerably when lowering the time step.

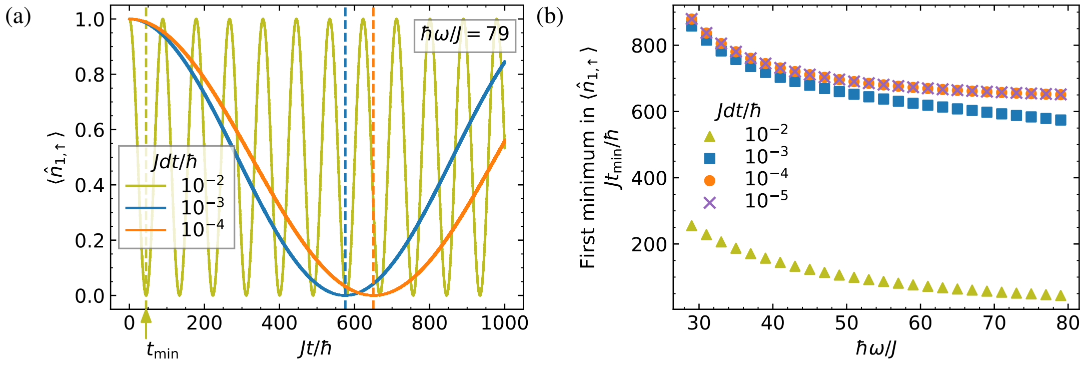

Figure 3.2: Single fermion case: Convergence of the numerics for small stepsizes. (a) Sample time evolution of a single fermion starting at $j = 1$ for different dt. The first minimum $t_{\min}$ is depicted by the vertical dashed lines. (b) Systematic comparison of the minima $t_{\min}$ for different dt within a wider parameter set.

To quantify this, we plot the time t_{min}, where the occupation $\langle \hat{n}_{1,\uparrow} \rangle$ first reaches 0 for different stepsizes dt and driving frequencies ω in figure 3.2(b). For higher driving frequencies, the numerics drift apart further, since the Hamiltonian $\hat{H}(t) \propto \sin(\omega t)$ changes more drastically.

Figure 3.3 shows the same kind of plots for the case of two fermions. Here, the numerics are a little more stable than in the single particle case.

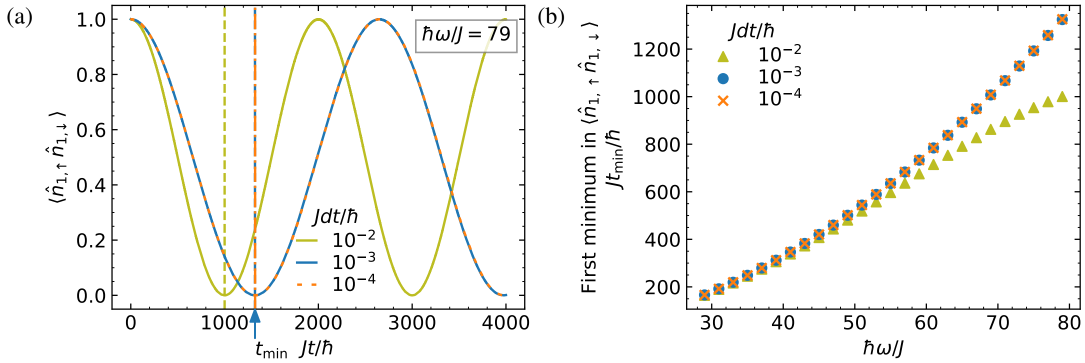

Figure 3.3: Two fermion case: Convergence of the numerics for small stepsizes. (a) Sample time evolution of a fermion pair starting at $j = 1$ for different dt. The first minimum t_{min} is depicted by the vertical dashed lines. (b) Systematic comparison of the minima t_{min} for different dt within a wider parameter set. Here, $U/J = -8$.

In both figures 3.2 and 3.3, the numerics seem well converged for $dt \lesssim 10^{-4}\hbar/J$. It should be noted that this method to choose dt is imperfect, since we only show the convergence for times $t \lesssim 1400\hbar/J$, but will later use numerical calculations for $tJ/\hbar$ in the ten thousands. On the other hand, figures 3.2 and 3.3 show the convergence for frequencies that are above most of those used later. Combining these effects and choosing dt with a safety margin should yield considerably accurate results. Having the program runtime in mind as well, all of the following calculations have been done with $dt = 10^{-4}\hbar/J$.

3.2 High-Frequency Approximation

We now want to move on to the underlying effective description of the driven Hamiltonian $\hat{H}(t)$ according to Floquet, which we have already seen first signs of in the numerical solution, e. g. in figure 3.1. For Hubbard type models, it is generally hard to find an exact form of $\hat{H}_{\mathrm{F}}$ [8], but as discussed in section 2.2.4 we can compute it approximately in orders of the inverse driving frequency ω^{-1}. Before doing, so we will apply a unitary gauge transformation

$$\hat{H}(t) \longrightarrow \hat{H}_{\mathrm{G}}(t) = \hat{U}_{\mathrm{G}}^{\dagger}(t)\hat{H}(t)\hat{U}_{\mathrm{G}}(t) - i\hbar\hat{U}_{\mathrm{G}}^{\dagger}(t)\dot{\hat{U}}_{\mathrm{G}}(t), \tag{3.4}$$

with $\hat{U}_{\mathrm{G}}(t) = \exp\left(i\frac{\kappa}{2\hbar\omega}\cos(\omega t)\sum_{\sigma}\left(-\hat{n}_{1,\sigma} + \hat{n}_{2,\sigma}\right)\right)$ to the model from equation 3.2. This is equivalent to transforming $|\psi(t)\rangle \longrightarrow |\psi(t)\rangle_{\mathrm{G}} = \hat{U}_{\mathrm{G}}^{\dagger}(t)\,|\psi(t)\rangle$[1]. The argument of the exponential is chosen, such that the second term in equation 3.4 cancels the driving term $\propto \sin(\omega t)$ in $\hat{H}(t)$. This way $\hat{H}_{\mathrm{G}}(t)$ only depends on $\kappa/\hbar\omega$ and not on κ alone, which is useful since the dynamics will turn out to appear at scales where $\kappa/\hbar\omega$ is fixed. Using a version of the Baker-Campbell-Hausdorff formula [25]

---

[1] In fact, $\hat{H}_{\mathrm{G}}(t)$ is chosen such that it describes the time evolution of the transformed states $|\psi(t)\rangle_{\mathrm{G}}$ like $i\hbar\mathrm{d}_t\,|\psi(t)\rangle_{\mathrm{G}} = \hat{H}_{\mathrm{G}}(t)\,|\psi(t)\rangle_{\mathrm{G}}$.

$$\mathrm{e}^{i\lambda\hat{G}}\hat{A}\mathrm{e}^{-i\lambda\hat{G}} = \sum_{n=0}^{\infty}\frac{(i\lambda)^n}{n!}\underbrace{[\hat{G},[\hat{G},...[\hat{G}}_{n\text{-times}},\hat{A}]...]]$$

for operators $\hat{A}$ and $\hat{G}$, we find

$$\begin{aligned}\hat{U}_{\mathrm{G}}(t)^{\dagger}\hat{c}^{\dagger}_{1,\sigma}\hat{c}_{2,\sigma}\hat{U}_{\mathrm{G}}(t) &= \exp\Big(-i\frac{K}{\hbar\omega}\cos(\omega t)\Big)\cdot\hat{c}^{\dagger}_{1,\sigma}\hat{c}_{2,\sigma} \quad \text{and}\\ \hat{U}_{\mathrm{G}}(t)^{\dagger}\hat{c}^{\dagger}_{2,\sigma}\hat{c}_{1,\sigma}\hat{U}_{\mathrm{G}}(t) &= \exp\Big(i\frac{K}{\hbar\omega}\cos(\omega t)\Big)\cdot\hat{c}^{\dagger}_{2,\sigma}\hat{c}_{1,\sigma}\ .\end{aligned}$$

With the Fourier expansion $\exp(i\lambda\sin(x)) = \sum_{k=-\infty}^{\infty}\mathcal{J}_k(\lambda)\exp(ikx)$, where $\mathcal{J}_k(\lambda)$ denotes the k-th Bessel function evaluated at λ, the gauge transformed Hamiltonian can be reduced to

$$\hat{H}_{\mathrm{G}}(t) = -J\sum_{k=-\infty}^{\infty}\mathcal{J}_k\left(\frac{K}{\hbar\omega}\right)i^k\exp(ik\omega t)\cdot\sum_{\sigma}\left(\hat{c}^{\dagger}_{1,\sigma}\hat{c}_{2,\sigma} + (-1)^k\hat{c}^{\dagger}_{2,\sigma}\hat{c}_{1,\sigma}\right) + U\left(\hat{n}_{1,\uparrow}\hat{n}_{1,\downarrow} + \hat{n}_{2,\uparrow}\hat{n}_{2,\downarrow}\right),$$

According to section 2.2.4, the effective Hamiltonian $\hat{H}_{\mathrm{F}}$ for $\hat{H}_{\mathrm{G}}(t)$ can now be calculated with the Fourier components $\hat{H}_{\mathrm{m}}$ which can be read off of $\hat{H}_{\mathrm{G}}(t)$ as the coefficients to $\exp(im\omega t)$. To first order, $\hat{H}_{\mathrm{F}}$ can be written down as

$$\begin{aligned}\hat{H}^{[1]}_{\mathrm{F}} = \hat{H}_0 = -J^{[1]}_{\mathrm{eff}}\sum_{\sigma}\left(\hat{c}^{\dagger}_{1,\sigma}\hat{c}_{2,\sigma} + h.c.\right) + U\left(\hat{n}_{1,\uparrow}\hat{n}_{1,\downarrow} + \hat{n}_{2,\uparrow}\hat{n}_{2,\downarrow}\right)\ ,\\ \text{with}\quad J^{[1]}_{\mathrm{eff}} = J\mathcal{J}_0\left(\frac{K}{\hbar\omega}\right)\ .\end{aligned} \tag{3.5}$$

Here, the instructive nature of the effective Hamiltonian becomes apparent. For sufficiently high driving frequencies the driven model just resembles the form of the static Hubbard Model (cf. eq. 3.1) with a modified hopping amplitude $J \longrightarrow J^{[1]}_{\mathrm{eff}}$ which makes it very easy to analyse since all the results from the static case just carry over. This stays true even to second order. $\hat{H}^{(2)}_{\mathrm{F}}$ vanishes identically, since $[\hat{H}_m, \hat{H}_{-m}] = 0$. Only to third order we obtain corrections

$$\begin{aligned}\hat{H}^{(3)}_{\mathrm{F}} = &- W_{\mathrm{i}}\left(\hat{n}_{1,\uparrow}\hat{n}_{1,\downarrow} + \hat{n}_{2,\uparrow}\hat{n}_{2,\downarrow}\right) + W_{\mathrm{k}}\sum_{\sigma}\left(\hat{c}^{\dagger}_{1,\sigma}\hat{c}_{2,\sigma} + h.c.\right)\\ &+ W_{\mathrm{p}}\left(\hat{c}^{\dagger}_{1,\uparrow}\hat{c}^{\dagger}_{1,\downarrow}\hat{c}_{2,\downarrow}\hat{c}_{2,\uparrow} + h.c.\right) + W_{\mathrm{i}}\sum_{\sigma}\left(\hat{c}^{\dagger}_{1,\sigma}\hat{c}^{\dagger}_{2,\overline{\sigma}}\hat{c}_{1,\overline{\sigma}}\hat{c}_{2,\sigma} + \hat{n}_{1,\sigma}\hat{n}_{2,\overline{\sigma}}\right),\end{aligned}$$

where $\overline{\sigma}$ denotes the opposite spin direction to σ and where

$$\begin{aligned}W_{\mathrm{i}} &= 2\frac{J^2U}{(\hbar\omega)^2}\sum_{m\neq 0}\frac{\mathcal{J}_m^2}{m^2}\\ W_{\mathrm{k}} &= 4\frac{J^3}{(\hbar\omega)^2}\sum_{m,\mathrm{odd}}\left[\frac{\mathcal{J}_0\mathcal{J}_m^2}{2m^2} - \sum_{m'\neq 0,m}(-1)^{m'}\frac{\mathcal{J}_m\mathcal{J}_{m-m'}\mathcal{J}_{m'}}{3m'm}\right]\\ W_{\mathrm{p}} &= -2\frac{J^2U}{(\hbar\omega)^2}\sum_{m\neq 0}(-1)^m\frac{\mathcal{J}_m^2}{m^2}.\end{aligned} \tag{3.6}$$

Note that $\mathcal{J}_m \equiv \mathcal{J}_m\left(\frac{\kappa}{\hbar\omega}\right)$ for the m-th Bessel function evaluated at $\kappa/\hbar\omega$ has been abbreviated for readability.

The full third order effective Hamiltonian is now given by

$$\begin{aligned}
\hat{H}_{\mathrm{F}}^{[3]} = -J_{\mathrm{eff}}^{[3]} \sum_{\sigma} \left(\hat{c}_{1,\sigma}^{\dagger}\hat{c}_{2,\sigma} + h.c.\right) &+ (U - W_{\mathrm{i}}) \left(\hat{n}_{1,\uparrow}\hat{n}_{1,\downarrow} + \hat{n}_{2,\uparrow}\hat{n}_{2,\downarrow}\right) \\
&+ J_{\mathrm{pair}}^{[3]} \left(\hat{c}_{1,\uparrow}^{\dagger}\hat{c}_{1,\downarrow}^{\dagger}\hat{c}_{2,\downarrow}\hat{c}_{2,\uparrow} + h.c.\right) \\
&+ W_{\mathrm{i}} \sum_{\sigma} \left(\hat{c}_{1,\sigma}^{\dagger}\hat{c}_{2,\bar{\sigma}}^{\dagger}\hat{c}_{1,\bar{\sigma}}\hat{c}_{2,\sigma} + \hat{n}_{1,\sigma}\hat{n}_{2,\bar{\sigma}}\right) , \\
\text{with} \quad J_{\mathrm{eff}}^{[3]} = J\mathcal{J}_0\left(\frac{\kappa}{\hbar\omega}\right) - W_{\mathrm{k}} &\quad \text{and } J_{\mathrm{pair}}^{[3]} = W_{\mathrm{p}} .
\end{aligned} \tag{3.7}$$

We find that if we restrict ourselves to the single fermion case, only the first two terms contribute and $\hat{H}_{\mathrm{F}}^{[3]}$ still resembles the static model, just with modified parameters J and U. With more particles, there are additional terms to interpret. The third term in equation 3.7 effectively adds hopping of two opposing spin fermions in pairs with an amplitude $J_{\mathrm{pair}}^{[3]}$. Lastly, the fourth and fifth terms add energies W_{i} related to spin flips and the interaction of opposite spins at different sites respectively.

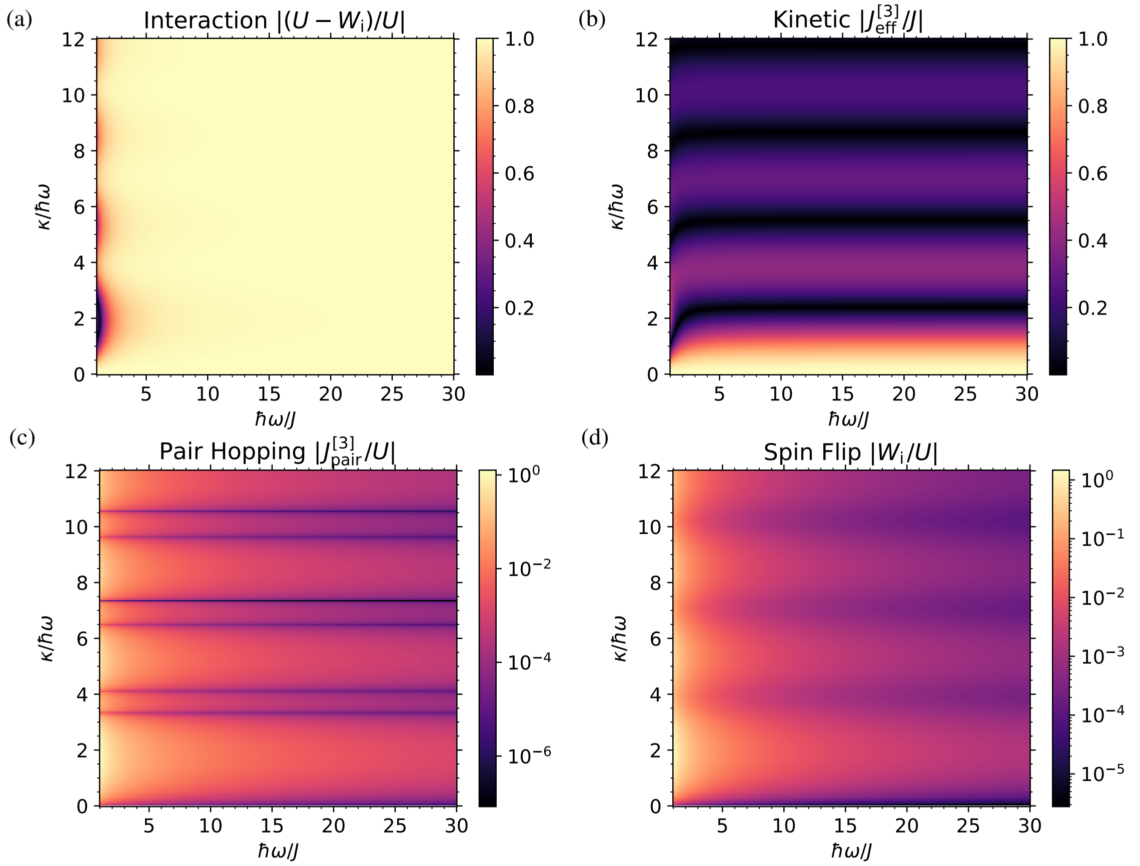

Figure 3.4: (a) Interaction, (b) kinetic energy, (c) pair hopping, (d) spin flip in the third order effective Hamiltonian $\hat{H}_{\mathrm{F}}^{[3]}$. Note the different energy scales, (a), (c) and (d) are in units of U, (b) is scaled by J.

The parameters of the third order effective model are visualized in figure 3.4. We will soon see that the high-frequency approximation will only really be accurate for frequencies $\hbar\omega$ much greater then the energy scales J and U of the system

3.2.1 Verifying the 1st Order

Since the first order just resembles the static model we can easily compare the numerics with the results of the static model we have already computed in section 2.1. The idea is to start with the static-model ground state that we found in section 2.1.1. If we now evolve the system while adiabatically turning on the driving, i. e. slowly ramping up κ from an initial value 0, the initial state should follow the ground state of the effective model. We can then watch one observable as it follows the effective prediction, i. e. the kinetic energy in the state from equation 2.3 with $J \longrightarrow J_{\text{eff}}^{[1]}$. Before they are directly comparable, the evolved driven ground state needs to be transformed into the gauge we introduced in section 3.2. This is done by applying $\hat{U}_{\text{G}}^{\dagger}(t)$ to the state at each step before the kinetic energy is extracted.

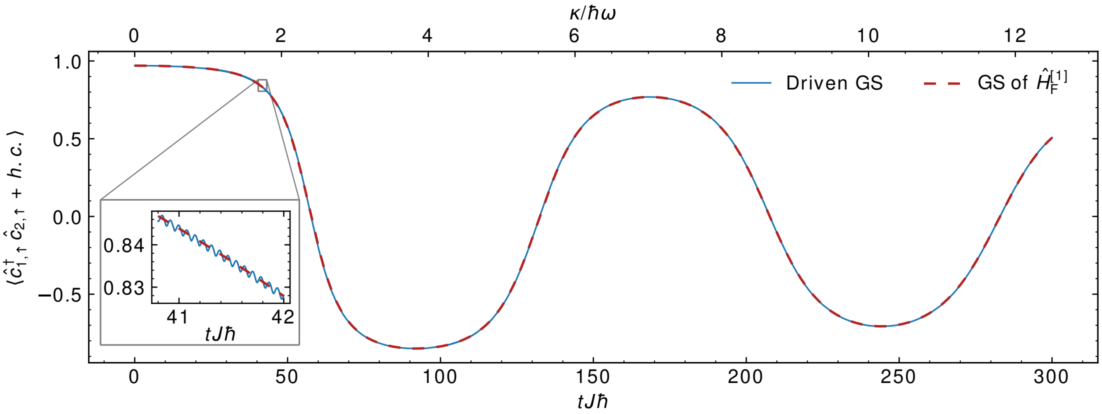

Figure 3.5: Starting with the static model ground state the driving κ is linearly ramped up in time from 0 to $\kappa = 12.5 \cdot \hbar\omega$ (see upper x-axis). The kinetic energy $\langle \hat{c}_{1,\sigma}^{\dagger}\hat{c}_{2,\sigma} + h.c.\rangle$ of the resulting state is compared to the kinetic energy of the first order effective model ground state. The upper x-axis shows the current driving amplitude κ at each point in the evolution. Here, $\hbar\omega/J = 40$ and $U/J = 1$.

The resulting comparison is depicted in figure 3.5. The driving strength was given in orders of $\hbar\omega$ to show the influence of the periodic Bessel function in $J_{\text{eff}}^{[1]}$. The driven ground state accurately follows the effective prediction up to small oscillations of period $T = 2\pi/\omega$ around the effective value (cf. zoomed-in view in fig. 3.5). These oscillations can be tuned to zero for very fast driving compared to the ramping time. We can conclude that the first order works very well in the given scenario.

3.2.2 Verifying the 3rd Order

We found that the second order vanishes. To third order the effective model from equation 3.7 does not in general resemble the static model anymore, so it does not make sense to compare it to the static ground state. We need to find another way of finding traces of $\hat{H}_{\text{F}}^{[3]}$ in the numerics.

Single-Fermion Oscillations

As a first test we can stick to the single fermion case. Now, all the extra terms in $\hat{H}_{\text{F}}^{[3]}$ do not contribute and we can again rely on previously derived analytical results. In section 2.1.1 we found that a single particle, objected to the static two-site model, oscillates back and forth between the two sites with a frequency of $\Omega_S = 2J/\hbar$. The same kind of oscillations appear in the effective model just with a modified frequency $\Omega_S^{[3]} = 2J_{\text{eff}}^{[3]}/\hbar$. Figure 3.6(a) shows the numerical time evolution of a single fermion for fixed $\kappa/\hbar\omega = 2.0$ and $\omega = 5J/\hbar$ with the driven model $\hat{H}(t)$ and the effective evolution from equation 2.7 with J_{eff}. The third order makes a visible correction to the oscillation frequency that matches well with the shaken model. Note that we do not need to change the gauge here, since $[\hat{U}_G(t), \hat{n}_{1,\sigma}] = 0$ and hence the observable $\langle \hat{n}_{1,\sigma} \rangle(t)$ coincides in both gauges.

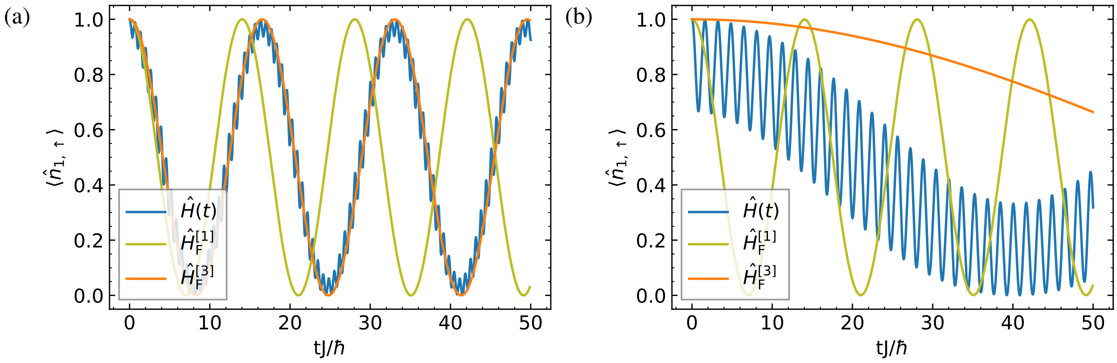

Figure 3.6: Comparison of the density oscillations of a fermion, w. l. o. g. of type spin up, starting at $j = 1$ in the full driven model $\hat{H}(t)$ with the approximate effective Hamiltonian to first $\hat{H}_F^{[1]}$ and third $\hat{H}_F^{[3]}$ order, for a driving amplitude of $\frac{\kappa}{\hbar\omega} = 2.0$. Only the density $\langle \hat{n}_1 \rangle$(t) at site$j = 1$ is shown. (a) $\hbar\omega/J = 5$ (b) $\hbar\omega/J = 2$.

Since this is our first direct comparison of the shaken model's time evolution to the effective descriptions, it is worth it to take a minute to understand what we see. Evidently there exist smaller underlying frequencies in the full numerical dynamics in figure 3.6(a) which the effective model does not explain. These can be better understood when looking at a Fourier transform $\mathcal{F}[\langle \hat{n}_1 \rangle]$ of the time evolution, see figure 3.7.

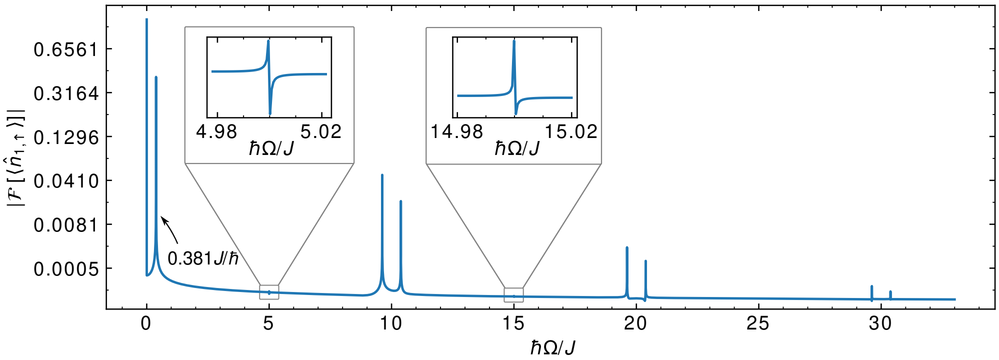

Figure 3.7: Fourier spectrum of the single fermion evolution in figure 3.6(a), where $\hbar\omega/J = 5$, $\kappa/\hbar\omega = 2.0$.

The first non-zero pronounced peak at $\Omega = 0.381J/\hbar$ matches well with the expectation $\Omega_S^{[3]} = 2J_{\text{eff}}^{[3]}/\hbar = 0.380J/\hbar$. To understand the full spectrum, note that the dynamics of a given state are essentially determined by the quasienergies $\epsilon_{nm} = \epsilon_n + m \cdot \hbar\omega$ of the system, where the ϵ_n

are the eigenvalues of $\hat{H}_\mathrm{F}$ and $m \in \mathbb{Z}$. The occurring frequencies in the Fourier transform correspond to differences in the quasienergies like

$$\Omega_{nmn'm'} = \frac{\epsilon_{nm} - \epsilon_{n'm'}}{\hbar} = \frac{\epsilon_n - \epsilon_{n'}}{\hbar} + (m - m')\omega\,. \tag{3.8}$$

Their amplitudes in the spectrum are related to the extend to which the different quasienergy excitations are included in the state. From equation 3.8 one can infer that the spectrum consists of frequencies $\Omega_{nn'} = (\epsilon_n - \epsilon_{n'})/\hbar$ which repeat in steps of ω. Turning back to figure 3.7, we can find the peak at $\Omega = 0$, corresponding to all Ω_{nmnm}, again at $\Omega = m \cdot 5J/\hbar$, though with a much smaller amplitude, see the zoomed-in plots. The peak we discussed earlier at $\Omega = 0.381J/\hbar$ corresponds to $(+J_\mathrm{eff}^{[3]} - (-J_\mathrm{eff}^{[3]}))/\hbar$, since the eigenvalues ϵ_n of the third-order effective Hamiltonian in the single particle case are given by $\pm J_\mathrm{eff}^{[3]}$. There is another one we cannot see at $(-J_\mathrm{eff}^{[3]} - (+J_\mathrm{eff}^{[3]}))/\hbar = -0.381J/\hbar$. We expect to find both of these again after full steps of ω. We can see that in figure 3.7 by the pairs of lines at 10 ± 0.381, 20 ± 0.381 and 30 ± 0.381. However, these only amount to half of the repeated lines, all the frequencies $m \cdot 5 \pm 0.381$ with m odd are missing. This effect appeared in all the single-fermion calculations. An intuitive explanation for this has yet to be found. It is also neither known whether the lines are missing completely or are just strongly damped.

Returning to the comparison, the numerics deviate strongly from the high-frequency approximations for lower driving frequencies, see figure 3.6(b) with $\omega = 2J/\hbar$ in two profound ways: first, the dominating oscillation frequency does not coincide with the effective prediction, and second, the underlying frequencies get stronger and can longer be neglected.

For a more sophisticated comparison of the former we again turn to the Fourier transform $\mathcal{F}[\langle\hat{n}_1\rangle]$. Figure 3.8(a) shows the first non-zero frequency $\Omega_\mathrm{S,min}$ in the spectrum (corresponding to pronounced peak in figure 3.7) for different driving strengths and frequencies. Note the apparent similarity to figure 3.4(b) which is a very good indicator that the third order works well since $\Omega_\mathrm{S}^{[3]} \propto J_\mathrm{eff}^{[3]}$. Figure 3.8(b) shows the relative deviation of the numerical result to the third order. Apart from two horizontal lines, corresponding to roots of $J_\mathrm{eff}^{[3]}$ – which should be handled with care because of the limited resolution in the numerical Fourier transform – the third order works very well for $\omega \gtrsim 5J/\hbar$. For lower ω the high frequency approximation mostly overestimates the numerics.

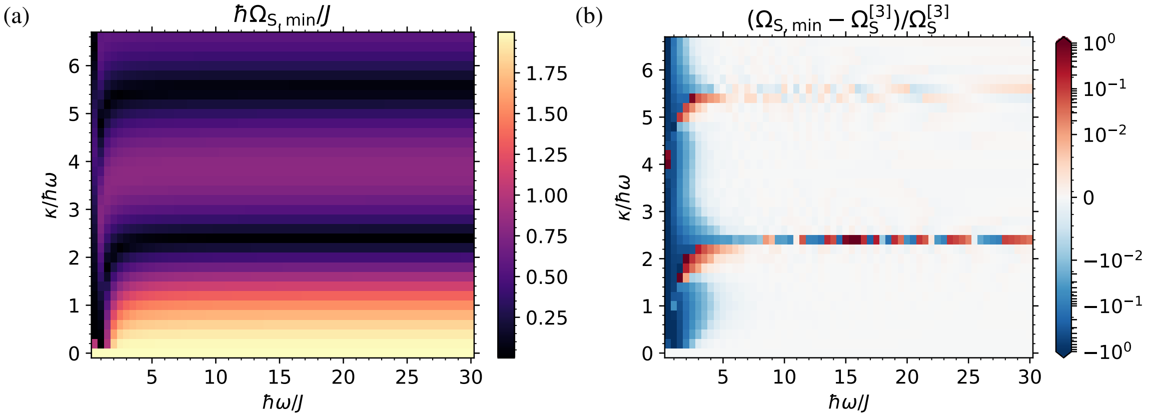

Figure 3.8: (a) Lowest non-zero frequency $\Omega_\mathrm{S,min}$ in the Fourier spectra $\mathcal{F}[\langle\hat{n}_{1,\uparrow}\rangle]$. (b) Comparison with the third order effective expectation $\Omega_\mathrm{S}^{[3]} = 2J_\mathrm{eff}^{[3]}/\hbar$, cf. figure 3.4(b).

Pair Evolution

Working in the single particle case, we can only see the effects of W_k in $\hat{H}_\mathrm{F}^{[3]}$. To see the other terms from equation 3.7 we have to put another fermion into the system. A natural extension of the previous discussion is to start with a pair at site $j = 1$ and see how that evolves with $\langle \hat{n}_{1,\uparrow} \hat{n}_{1,\downarrow} \rangle (t)$. This also fulfils $[\hat{U}_\mathrm{G}(t), \hat{n}_{1,\uparrow} \hat{n}_{1,\downarrow}] = 0$ such that no change of gauge is needed. Figure 3.9 shows this for two different driving frequencies. $\kappa / \hbar\omega$ was set to 2.4 on purpose, tuning $J_\mathrm{eff}^{[3]}$ roughly to zero. This way, the dynamics we see are mostly determined by the other terms.

To find examples, where the approximation works well, it is already necessary to use much higher driving frequencies as previously. Figure 3.9(a) shows that the third order is a well-needed correction to the first at $\omega = 40J/\hbar$. But while the single-particle approximation worked well even for $\omega \gtrsim 5J/\hbar$, the two-fermion approximation breaks down much earlier, see figure 3.9(b). To first order, the single-fermion Hamiltonian's energy scale is of order J, while here the scale is $U = -8J$. This way, resonances where $\hbar\omega$ is close to the energy scale, at which the approximations necessarily break down, appear at higher frequencies.

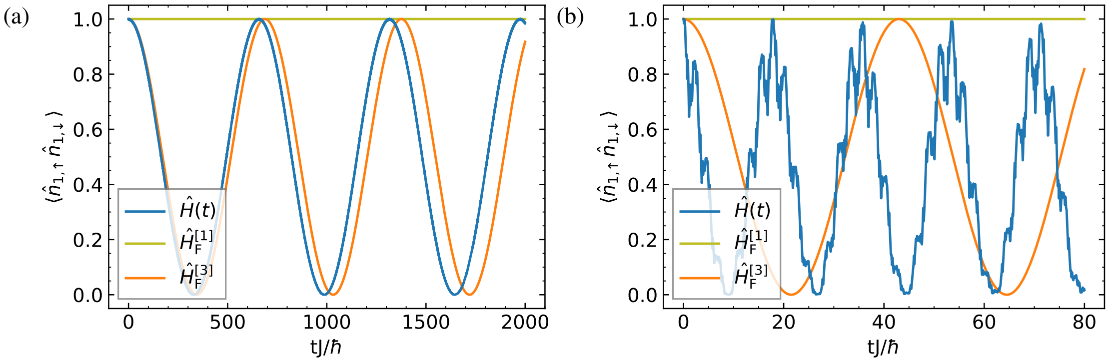

Figure 3.9: Time evolution of a fermion pair, starting at $j = 1$ in the full model $\hat{H}(t)$ and the effective descriptions. The effective time evolutions have been computed analytically, see appendix A. $\kappa / \hbar\omega = 2.4$ in both, (a) $\hbar\omega / J = 40$, (b) $\hbar\omega / J = 10$.

Again, it is instructive to take a quick look at a Fourier transform of the pair evolutions, see figure 3.10. According to figure 3.9(a), the third order is at least approximately suitable to describe the time evolution at the given driving frequency $\omega = 40J$. $\hat{H}_\mathrm{F}^{[3]}$ has eigenvalues

$$\begin{aligned} \epsilon_1 &= 0 \quad , \quad \epsilon_2 = U - W_\mathrm{i} - J_\mathrm{pair}^{[3]} , \\ \epsilon_3 &= \frac{1}{2} \left(U + W_\mathrm{i} + J_\mathrm{pair}^{[3]} + \sqrt{J_\mathrm{eff}^{[3]2} + \left(U - 3W_\mathrm{i} + J_\mathrm{pair}^{[3]} \right)^2} \right) \quad \text{and} \\ \epsilon_4 &= \frac{1}{2} \left(U + W_\mathrm{i} + J_\mathrm{pair}^{[3]} - \sqrt{J_\mathrm{eff}^{[3]2} + \left(U - 3W_\mathrm{i} + J_\mathrm{pair}^{[3]} \right)^2} \right) . \end{aligned} \tag{3.9}$$

With $\hbar\omega / J = 40$, $\kappa / \hbar\omega = 2.4$ and $U/J = -8$, this amounts to $\epsilon_1 = 0$, $\epsilon_2 = -7.989J$, $\epsilon_3 = -0.013J$ and $\epsilon_4 = -7.998J$. In the spectrum, we see four distinct lines, at $\Omega_1 = 0J$, $\Omega_2 = 0.009J/\hbar$, $\Omega_3 = 7.975J/\hbar$ and $\Omega_4 = 7.985J/\hbar$. The origin of the zero line is self-evident, the others can best be interpreted as

$\Omega_2 \mathrel{\hat{=}} \epsilon_2 - \epsilon_4 = 0.009J$, $\Omega_3 \mathrel{\hat{=}} \epsilon_3 - \epsilon_2 = 7.976J$ and $\Omega_4 \mathrel{\hat{=}} \epsilon_3 - \epsilon_4 = 7.985J$. Other combinations do not seem to appear. These four lines repeat in steps of ω in the spectrum. Additionally, all of them also have a negative counterpart which also repeats. These identifications should be treated with some care respecting the numerical error. Still, one can nicely explain the spectrum with the effective model.

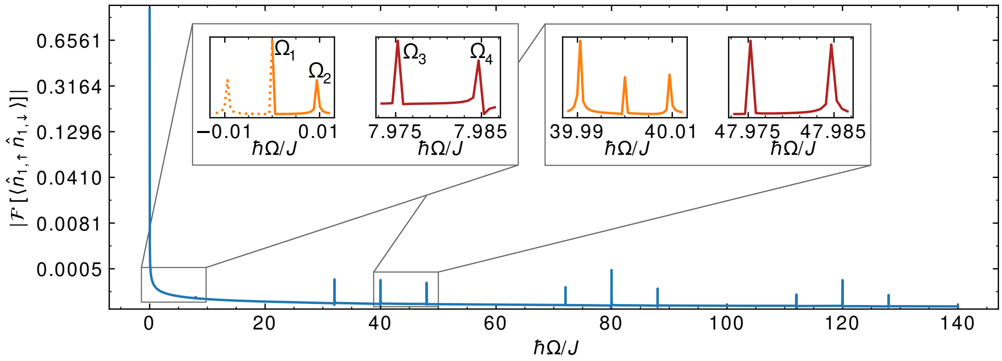

Figure 3.10: Fourier spectrum of the time evolution in figure 3.9(a). $U/J = -8$, $\hbar\omega/J = 40$ and $\kappa/\hbar\omega = 2.4$. Zoomed-in views of the same color help illustrate repeating peaks of the same quasienergy ϵ_n. The dotted lines have been mirrored from the positive frequencies to underline the repetition of the negative peak. At about $\hbar\Omega/J \approx 32$, there is a repetition of the negative counterpart of the two red peaks.

Figure 3.11(a) shows the position of the lowest non-zero peak in the spectra of different driving strengths and frequencies at $U/J = -20$. Nicely visible are the resonances at roughly $\hbar\omega = U/n$ ($n \in \mathbb{N}$). In the two-fermion case, we also have to be much more careful with multiple underlying frequencies occurring. Figure 3.11(b) compares that frequency to the lowest non-zero frequency $\Omega^{[3]}_{\mathrm{P,min}}$ in the third order effective model. Since it is much more complicated to give an analytical expression than in the single-fermion case, $\Omega^{[3]}_{\mathrm{P,min}}$ has been computed numerically from equation A.3. Here, one very thoroughly sees the impact of the resonances. In large areas around them the pair hopping is increased, only far away at high frequencies the third order matches the numerical results.

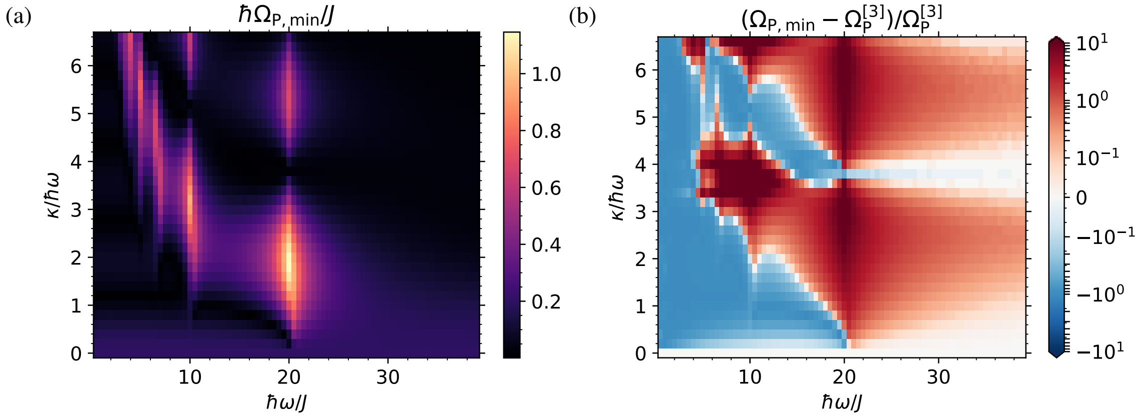

Figure 3.11: (a) Lowest non-zero frequency $\Omega_{\mathrm{S,min}}$ in the Fourier spectra $\mathcal{F}[\langle \hat{n}_{1,\uparrow}\hat{n}_{1,\downarrow}\rangle]$, (b) Comparison with the lowest non-zero frequency in the third order effective model $\Omega^{[3]}_{\mathrm{P}}$. $U/J = -20$ in both figures.

CHAPTER 4

Floquet Engineering the Model

We are now set up to work towards the final goal of this thesis: Engineering the parameters of the driven model $\hat{H}(t)$, given by eq. 3.2, such that the resulting effective system effectively contains 1) negligible single-particle dynamics coupled with 2) increased pair hopping. The former will turn out to be easily achievable since we found out in section 3.2 that the single particle dynamics are well described by $J_{\text{eff}}^{[3]}$, which can be tuned to zero analytically. The latter is more complicated since the high frequency approximation breaks down faster such that we will mostly have to rely on numerics.

This chapter builds up as follows: First, a general overview on where to look for parameters that achieve both is given in section 4.1. After lowering the single particle hopping in section 4.2, two potential regimes for increased pair hopping will be explored in 4.3, the high frequency regime in section 4.3.1 and inside the resonance region in section 4.3.2.

4.1 Where to Look

Whether we want to verify that our analytic methods to tune J_{eff} succeed, or we in pair hopping case have to rely heavily on the numerics, a method to extract J_{eff} or J_{pair}[1] from the numerics is needed.

We already successfully extracted J_{eff} from the numerics in section 3.2, cf. figures 3.8(a) and 3.4(b). Essentially, when evolving a single fermion, it will oscillate with a frequency $\Omega_S = 2J_{\text{eff}}/\hbar$, as long as the driven model resembles the static Hubbard model in the effective picture.

The pair dynamics are usually more complex. Yet, say we found some set of parameters for which the model is, at least approximately, effectively described by some idealized pair hopping Hamiltonian

$$\hat{H}_{\text{pair}} = J_{\text{pair}} \left(\hat{c}^\dagger_{1,\uparrow} \hat{c}^\dagger_{1,\downarrow} \hat{c}_{2,\downarrow} \hat{c}_{2,\uparrow} + h.c. \right) + U \left(\hat{n}_{1,\uparrow} \hat{n}_{1,\downarrow} + \hat{n}_{2,\uparrow} \hat{n}_{2,\downarrow} \right)$$

without single hopping or other dynamics breaking the pairs. Just like the Hubbard model features oscillations of single fermions between two sites with a frequency of $\Omega_S = 2J/\hbar$, $\hat{H}_{\text{pair}}$ gives rise to pair oscillations with $\Omega_P = 2J_{\text{pair}}/\hbar$. To see this, notice that $\hat{H}_{\text{pair}}$ conserves the total number of pairs $\hat{N}_{\text{pair}} = \hat{n}_{1,\uparrow}\hat{n}_{1,\downarrow} + \hat{n}_{2,\uparrow}\hat{n}_{2,\downarrow}$. Hence, in the case of one pair, we can reduce the Hilbert space to $\{|1100\rangle, |0011\rangle\}$, corresponding to the pair being at site 1 or 2, respectively. In this space,

$$\hat{H}_{\text{pair}} \doteq \begin{pmatrix} U & J_{\text{pair}} \\ J_{\text{pair}} & U \end{pmatrix} .$$

---

[1] $J_{\text{eff}}^{[3]}$ and $J_{\text{pair}}^{[3]}$ denote the single and pair hopping amplitudes of $\hat{H}_{\text{F}}^{[3]}$, while J_{eff} and J_{pair} will be used when referring to the respective matrix elements of the unknown exact $\hat{H}_{\text{F}}$ for arbitrary driving frequencies.

This deviates from equation 2.6 merely by a constant on the diagonal, which does not alter the dynamics. The resulting state at time t, after evolving an initial state $\left|\psi(t_0 = 0)\right\rangle = |1100\rangle$, can thus immediately be written down as

$$|\psi(t)\rangle = \cos\left(\frac{tJ_{\text{pair}}}{\hbar}\right)|1100\rangle - i\sin\left(\frac{tJ_{\text{pair}}}{\hbar}\right)|0011\rangle \ .$$

Hence, a pair initially located at $j = 1$ oscillates between the sites with a frequency $\Omega_\text{P} = 2J_\text{pair}/\hbar$.

The general procedure can now be stated as follows: Starting with a single fermion (or a fermion pair) at $j = 1$, we have to find regions in which the dynamics of $\langle\hat{n}_{1,\uparrow}\rangle$ ($\langle\hat{n}_{1,\uparrow}\hat{n}_{1,\downarrow}\rangle$) are predominantly described by a single frequency Ω_S (Ω_P). Then J_eff (J_pair) can be assumed to be directly proportional to this frequency. In these regions, one can then try to maximize Ω_P while keeping Ω_S low.

Figure 4.1 gives a first general overview on where this could be achieved. The chosen minimal non-zero frequency in the spectra nearly always has the highest amplitude, but is a little less prone to numerical error if two frequencies reach similar heights in the spectrum, which makes it a good candidate for Ω_P. It is important to stress here that figure 4.1(a) alone is not sufficient to assess the ratio $J_\text{pair}/J_\text{eff}$, since it does not evaluate whether the single frequency assumption is justified. Yet, it can be seen, that it should be fruitful to concentrate on the roots of $\Omega_\text{S}^{[3]} \propto J_\text{eff}^{[3]}$ (see the bright horizontal lines in figure 4.1(b)) of $\Omega_\text{S}^{[3]}$ and, with some care, around the resonances of Ω_P. We will concentrate on the first root around $\kappa/\hbar\omega = 2.4$, since in first computations it lead to more promising results than the root around $\kappa/\hbar\omega = 5.3$. This can at least approximately be understood, when looking at figure 3.4(c) in which the effective pair hoping decreases for higher $\kappa/\hbar\omega$, at least to third order.

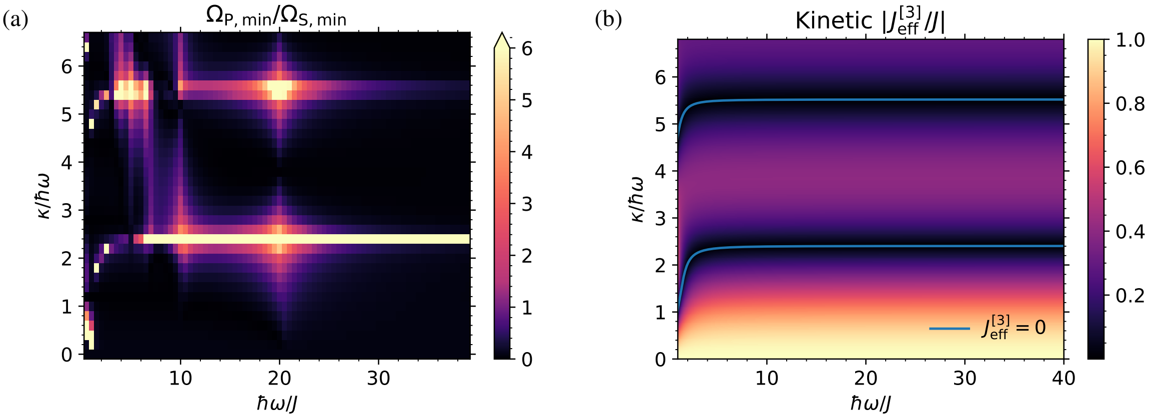

Figure 4.1: (a) Ratio of the lowest non-zero frequencies in the evolution of a pair and of a single fermion from figures 3.8(a) and 3.11(a). (b) $J_\text{eff}^{[3]}$ zoomed in from figure 3.4(b) with its root, see section 4.2.

4.2 Suppressing Single Fermion Hopping

Since it is the easiest to do and can be realized with strong effects on the ratio $J_\text{pair}/J_\text{eff}$, we will first minimize J_eff. From figure 3.8 we found that for a large set of driving frequencies, the resulting single-particle dynamics are well described by $\Omega_\text{S}^{[3]} = 2J_\text{eff}^{[3]}/\hbar$. This has an analytical root, which is determined by the condition

$$J_\text{eff}^{[3]} = 0 \ \Leftrightarrow \ J\mathcal{J}_0\left(\frac{\kappa_\text{min}}{\hbar\omega_\text{min}}\right) = W_\text{k} \, .$$

Suppressing the arguments $(\kappa/\hbar\omega)_{\text{min}}$ of the Bessel functions and using equation 3.6 for W_{k} we obtain

$$\frac{\hbar\omega_{\text{min}}}{J} = \sqrt{\frac{\mathcal{J}_0}{4\sum_{m,\text{odd}}\left[\frac{\mathcal{J}_0\mathcal{J}_m^2}{2m^2} - \sum_{m'\neq 0,m}(-1)^{m'}\frac{\mathcal{J}_m\mathcal{J}_{m-m'}\mathcal{J}_{m'}}{3m'm}\right]}}\,. \tag{4.1}$$

Comparing figure 4.1(b) with figure 4.1(a), the root follows roughly the line of high numerical $\Omega_{\text{P}}/\Omega_{\text{S}}$. To see how low J_{eff} can be tuned this way, we go through different ω and choose $\kappa/\hbar\omega$ for each one, such that the condition 4.1 is fulfilled. We can use the lowest non-zero frequency $\Omega_{\text{S,min}}$ in the Fourier spectrum of the evolution $\langle\hat{n}_{1,\uparrow}\rangle(t)$ to compare with $\Omega_{\text{S}}^{[3]}$. In the lower part of figure 4.2, we see that the numerics follow the root very well for $\omega \gtrsim 6J/\hbar$, as was to be expected, and then slowly grow.

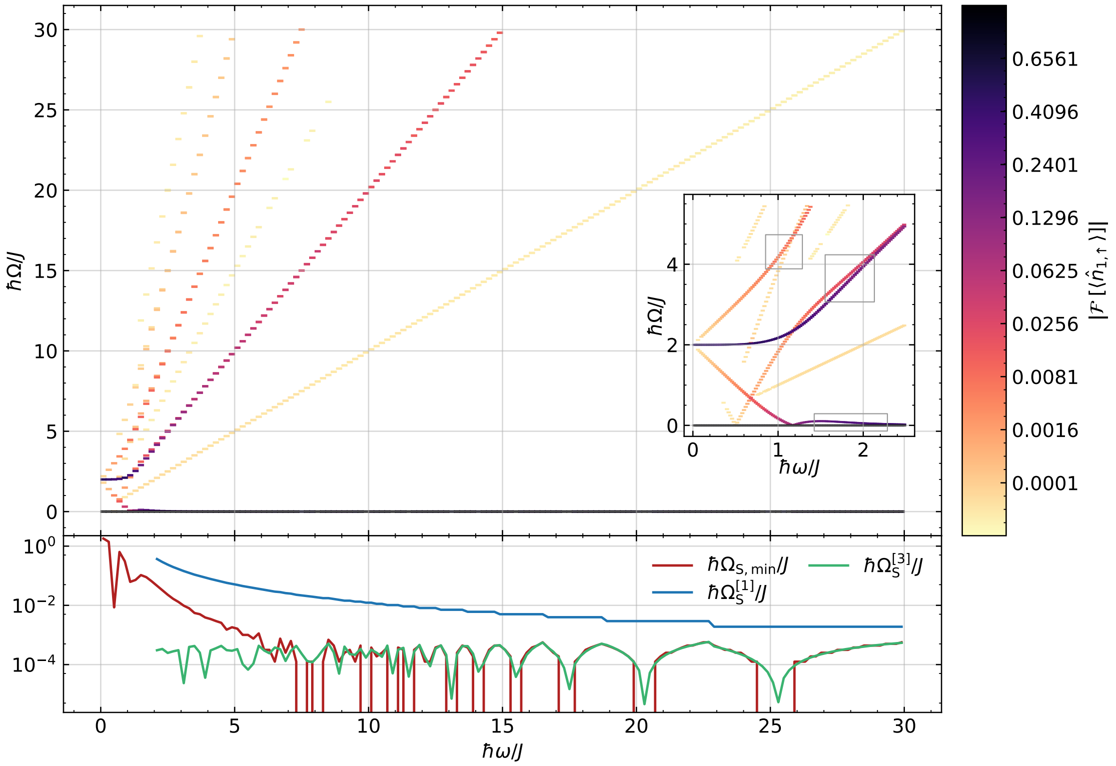

Figure 4.2: Peaks of the single (spin up) fermion Fourier spectra $|\mathcal{F}[\langle\hat{n}_{1,\uparrow}\rangle]|$ (upper panel) and lowest non-zero frequency $\Omega_{\text{S,min}}$ compared to effective models (lower panel). $\kappa/\hbar\omega$ is for each ω chosen such that $J_{\text{eff}}^{[3]} = 0$, i. e. it follows the condition 4.1. The jumps in $\Omega_{\text{S}}^{[1]}$ and finite, non-constant $\Omega_{\text{S}}^{[3]}$ are artifacts of $\kappa/\hbar\omega$ only being tuned to the third decimal place. The thickness of the lines is constant and has nothing to do with the resolution, which would otherwise be too low to see. Where $\Omega_{\text{S,min}}$ drops to zero, the lowest frequency peak could not be differentiated from $\Omega_{\text{S}} = 0$ at the given resolution of $\Delta\Omega = 6.28 \cdot 10^{-5} J/\hbar$.

The upper portion of figure 4.2 shows all the peaks in the spectra. A vertical cut corresponds to one spectrum like figure 3.7. The one frequency assumption is mostly justified, since the second highest amplitude frequency in the spectra is for the most part about $1/20$'th of the amplitude of $\Omega_{\text{S,min}}$. We can thus conclude, that we can generally tune $\Omega_{\text{S,min}} \leq 0.5 \cdot 10^{-3} J/\hbar$, i. e. $J_{\text{eff}} \leq 0.25 \cdot 10^{-3}$, but one should keep in mind that these results require us to tune $\kappa/\hbar\omega$ to the third decimal place.

It is worth it to understand the upper part of figure 4.2 as a continuation of the discussion in section 3.2.2. There we found peaks at $\Omega = n \cdot \omega$ and at $n \cdot \omega \pm 2J^{[3]}_{\text{eff}}/\hbar$ for m even in the single-particle spectrum. The grid lines help to identify the former as the diagonal lines in figure 4.2. Since we set $J^{[3]}_{\text{eff}} = 0$ the latter are hard to distinguish, but they can be seen when the two lines start to deviate from the effective prediction and disentangle for low ω in the marked regions in the zoomed-in view. For $\omega \to 0$ all lines converge to $\Omega = 2J/\hbar$ and $\Omega = 0$, corresponding to the static non-driven expectation[2]. For $\omega \to \infty$ they converge to the first order $n \cdot \omega \pm 2J^{[1]}_{\text{eff}}/\hbar$, where again $J^{[1]}_{\text{eff}} = 0$.

4.3 Enhancing Pair Hopping

We will now move on to maximizing J_{pair} while staying within the first root of $J^{[3]}_{\text{eff}}$. We could simply work in the high-frequency regime, where $\hat{H}^{[3]}_{\text{F}}$ is sufficient to describe the system, but judging from figure 3.11 we might reach higher values of J_{pair} with lower ω, particularly around the resonances.

Figure 4.3 is the analogue of figure 4.2, where we now started with a particle pair at $j = 1$ and compute the Fourier spectrum of its time evolution. Again, one vertical slice corresponds to the spectrum at one driving frequency ω, with corresponding κ chosen, such that $J^{[3]}_{\text{eff}} = 0$.

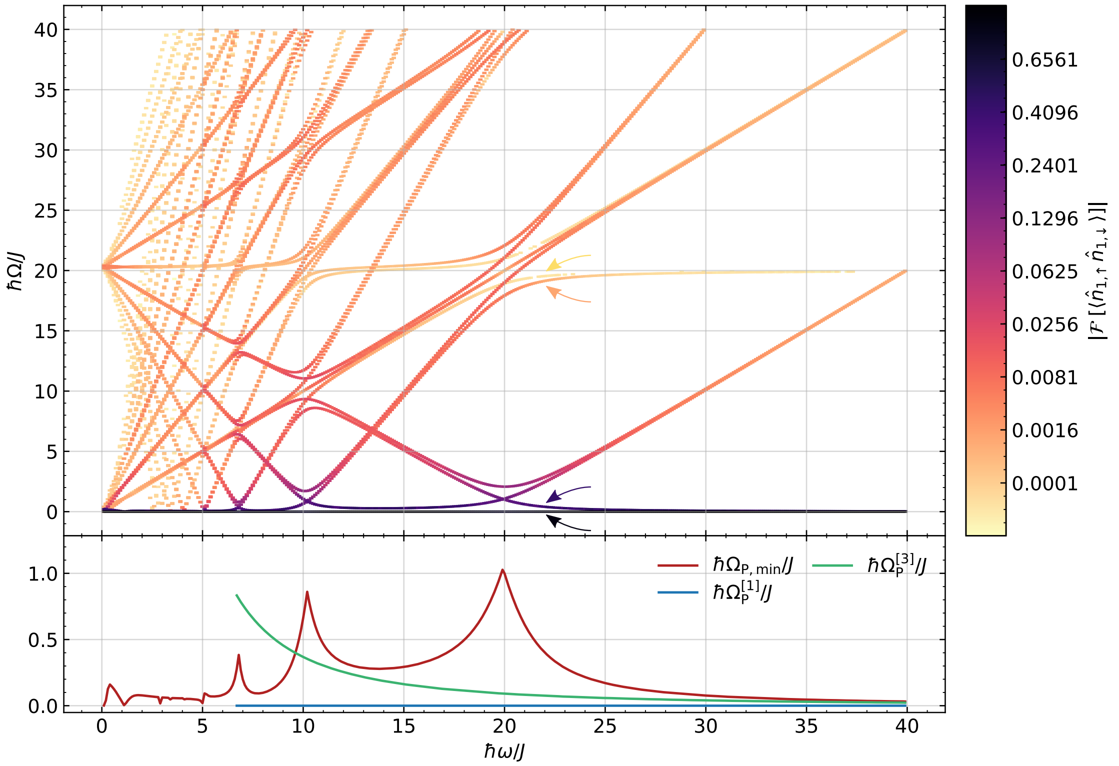

Figure 4.3: (Upper panel) Frequencies Ω in the time evolution of a fermion pair. (Lower panel) Lowest non-zero frequency $\Omega_{\text{P,min}}$ in the spectrum compared to effective models. The effective frequencies have been computed numerically from the analytical time evolution in appendix A. The interaction energy is $U = -20J$. $\frac{\kappa}{\hbar\omega}$ is chosen such that $J^{[3]}_{\text{eff}} = 0$. The resolution is $\Delta\Omega = 6.28 \cdot 10^{-4} J/\hbar$.

---

[2] Which can either be inferred from eq. 2.7 or from equation 3.8 with $\epsilon_n \to \pm J$.

We can see four unique lines in the plot, which are easiest to identify when $\omega \to \infty$. The effective model converges to $\hat{H}_\mathrm{F}^{[1]}$ which just resembles the static model with $J_\mathrm{eff} \approx 0$. From section 2.1.1, the quasienergy eigenvalues converge to $\epsilon_1 = \epsilon_3 = 0$ and $\epsilon_2 = \epsilon_4 = U = -20J$. These combine to $\Omega = 0$ and $\Omega = 20J/\hbar$. In figure 4.3, we see these as two horizontal lines for high ω that split up in two each for lower ω. With the four lines that emerge (see arrows in fig. 4.3), the rest of the spectrum can be explained merely by repetition ($\pm n \cdot \hbar\omega$) of them or their negative counterparts. The reader is asked to confirm this for himself by identifying lines in figure 4.3 and tracing them back to one of the basic four.

The resonances at $\hbar\omega \approx U/n$ are also well visible. They form the discontinuities in $\Omega_\mathrm{P,min}$ and make up the tips of cone-like structures in the full spectrum, corresponding to crossings of the quasienergies.

Influence of the Interaction Energy U

Having seen and understood one spectrum, we will first have a look at a few more to understand their more general structure and to see the influence of the interaction U. Figure 4.4 gives a look at $U = -8J$. This spectrum has a very similar structure compared to $U = -20J$ in figure 4.3. Again the resonances are visible, and we can identify the four lines, two of which converge to 0, and the other two converge to roughly $8J/\hbar$ in the high-frequency limit. Since they split up more then in figure 4.3 it is also well visible how all lines converge to four values of Ω for $\omega \to 0$ (see arrows in fig. 4.4) that correspond to differences in the energies $E_1^{(2,0)} = 0$, $E_2^{(2,0)} = -8J$, $E_3^{(2,0)} = -8.47J$ and $E_4^{(2,0)} = 0.47J$ of the static model (cf. section 2.1.1). Another difference is that compared to $U = -20J$, $\Omega_\mathrm{P,min}$ does not fall off as quickly around the resonances, especially in between the highest two.

Figure 4.5(a) shows the spectrum for $U = +8J$ to explore the effect of positive U. For U in the order of magnitude of J, see figures 4.5(a) and 4.5(c), where $U = -2J$ and $-0.5J$ respectively.

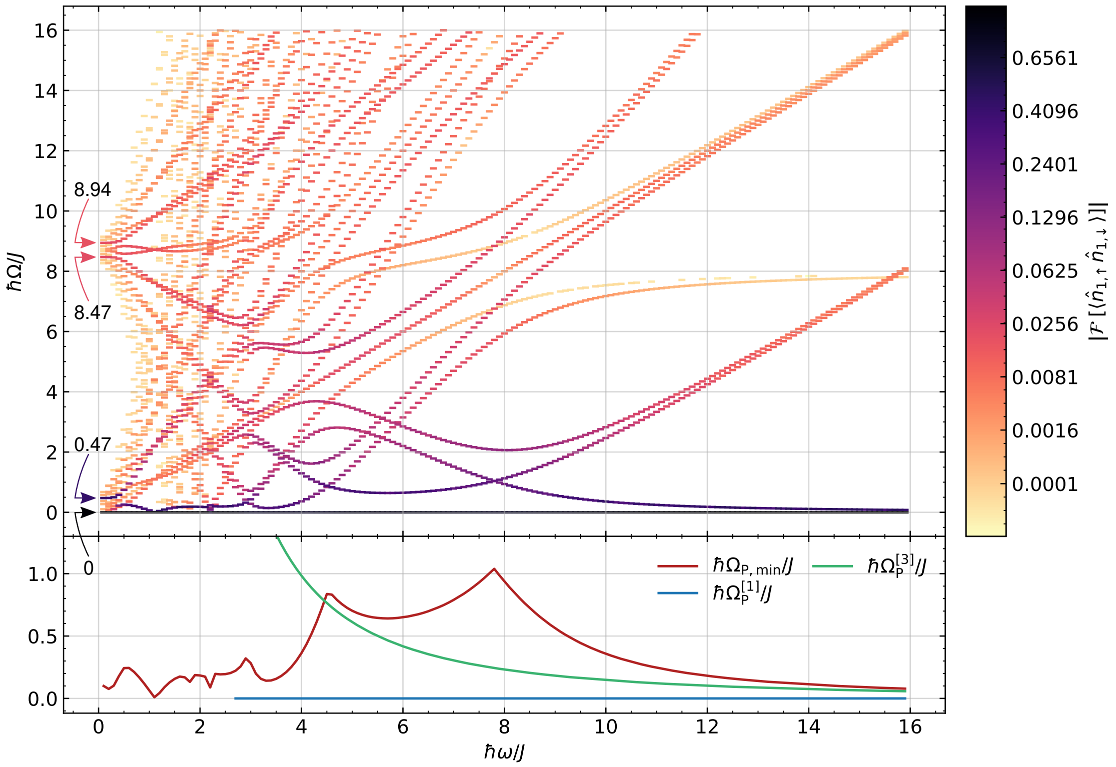

Figure 4.4: (Upper panel) Frequencies Ω in the time evolution of a fermion pair. (Lower panel) Lowest non-zero frequency $\Omega_\mathrm{P,min}$ in the spectrum compared to effective models. Analogous to figure 4.3 but for $U = -8J$.

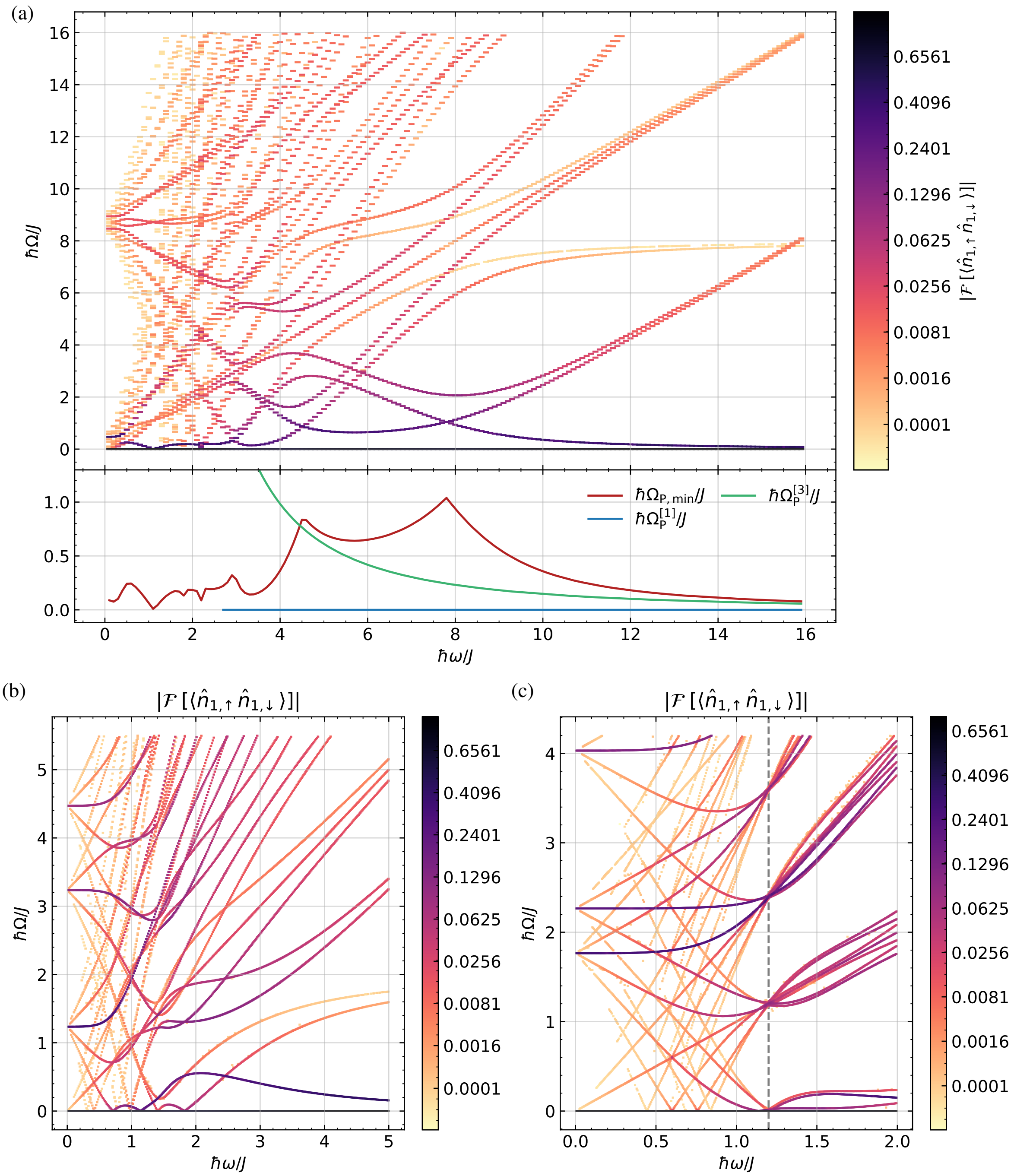

Figure 4.5: (a) (Upper panel) Frequencies Ω in the time evolution of a fermion pair. (Lower panel) Lowest non-zero frequency $\Omega_{\mathrm{P,min}}$ in the spectrum compared to effective models. Analogous to figure 4.4 but for $U = +8J$. (b), (c) Pair evolution spectra for $U/J = -2$ and $U/J = -0.5$ respectively. The vertical dashed line in (c) marks the flattening of the bands at $\hbar\omega/J = 1.20$ as discussed in the text.

The first thing we notice is that the spectrum seems to be completely independent of the sign of U, figure 4.5(a) ($U = +8J$) looks identical to 4.4 ($U = -8J$). We can understand that to third order in the high frequency limit, where all the quasienergies (cf. eq. 3.9) simply change sign under the transformation $U \longrightarrow -U$ [3] and hence, the Fourier spectrum does not change. The fact that it does not depend on the sign of U even for low frequencies hints at a general symmetry in the model. The form of this symmetry has not been found yet and remains to be examined further.

From figures 4.5(b) and 4.5(c), we see that for low interaction U the spectra differ considerably from high U. There is no defined structure for the minimum frequencies, and these frequencies do not dominate; rather, there are many frequencies of similar magnitude. Figure 4.5(c) seems especially interesting since all the bands flatten at $\omega \approx 1.20J/\hbar$. An explanation for this has yet to be found, but we will have no chance of applying the one-frequency assumption here anyway.

With respect to our goal of maximizing J_{pair}, the spectra tell us sets of parameters where $\Omega_{\text{P,min}}$ is high, but also that whenever we get close to the interesting resonance regimes of large $\Omega_{\text{P,min}}$, there are always multiple other frequencies with high amplitudes. We can thus not directly look at a resonance and deduce that we have found high J_{pair}. To quantify this effect, it is useful to look at how likely the pairs are to stay together in their dynamics, which can be deduced from the minimum in the time evolution of the amount of pairs $\langle \hat{N}_{\text{pair}} \rangle_{\text{min}} = \langle \hat{n}_{1,\uparrow}\hat{n}_{1,\downarrow} + \hat{n}_{2,\uparrow}\hat{n}_{2,\downarrow} \rangle_{\text{min}}$. Terms in the effective Hamiltonian that make the evolution deviate from the one frequency assumption also break the pairs. This is highly relevant to us, because the conservation of the pairs is an important symmetry of the model we are trying to reproduce, protecting the topological Majorana modes [15, 16]. Figure 4.6(a) shows $\langle \hat{N}_{\text{pair}} \rangle_{\text{min}}$ for $U = -20J$ for different ω. For comparison, $\Omega_{\text{P,min}}$ has also been added. All the resonance features can also be seen in the pair breaking. Figure 4.6(b) shows a more general look at this. Comparing it to figure 3.11(a), we can conclude that the pairs are not conserved at the resonances.

From the data we gathered, there are two regions of potentially high J_{pair} to explore more carefully now. First, at high ω, the pairs stick together and we can apply the one-frequency assumption (see figure 4.6(a)). And second, the resonance regime: At the resonances the pair is breaking, but there there is a small region in between the two highest resonances in which we might succeed.

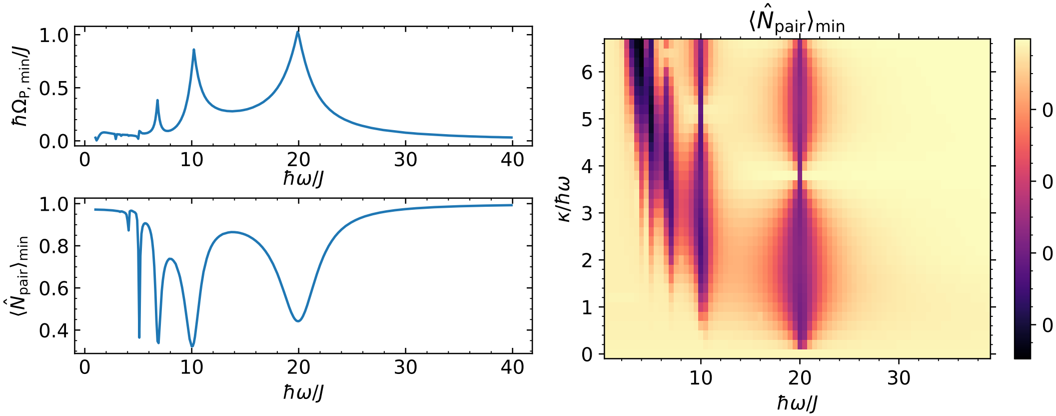
(a)

(b)

Figure 4.6: (a) Comparison of the minimum number of total pairs $\langle \hat{N}_{\text{pair}} \rangle_{\text{min}}$ in the pair evolution (lower panel) with the oscillation frequency (upper panel) for $U = -20J$. (b) $\langle \hat{N}_{\text{pair}} \rangle_{\text{min}}$ for different values of $\kappa/\hbar\omega$ and ω, in direct comparison to fig. 3.11(a).

---

[3] If we remember that, from eq. 3.6, $W_{\text{i}} \propto U$ and $J^{[3]}_{\text{pair}} \propto U$ and we interchange the roles of ϵ_3 and ϵ_4.

4.3.1 High Frequency Regime

We have seen that for large ω the pairs do not break. Hence, in the third order effective model, the spin flip term proportional to W_i (cf. eq. 3.7) cannot contribute. Since we also set $J^{[3]}_\text{eff} = 0$, the third order essentially resembles the idealized pair hopping Hamiltonian $\hat{H}_\text{pair}$ we introduced in equation 4.1 with a pair hopping amplitude $J^{[3]}_\text{pair}$. In the high-frequency limit $\hbar\omega \gg U$ we thus expect clean cosine-shaped one-frequency oscillations of a fermion pair, which can also be seen in the numerics, e. g. for $U = -8J$ with $\hbar\omega = 22J$ in figure 4.7(a). This would provide ideal conditions for us, but the disadvantage is that the dominating frequency $\Omega_\text{P,min}$ is very small, e. g. $\Omega_\text{P,min} = 0.035J/\hbar$ in figure 4.7(a).

Looking at $J^{[3]}_\text{pair} = W_\text{p}$ from equation 3.6, there are two ways of increasing it while keeping $\kappa/\hbar\omega$ fixed: decreasing ω and increasing U. We can see the effect of the former in the rise of $\Omega_\text{P,min}$ in figure 4.4. We test for linear dependency of the latter in figure 4.8(a) by choosing a fixed high frequency $\hbar\omega = 40J$ and compare $\Omega_\text{P,min}$ to the $2J^{[3]}_\text{pair}/\hbar$ of the idealized model in figure 4.8(a). For completeness, the numerical $\Omega^{[3]}_\text{P}$ for the third order is given. The linearity is apparent for low U, but when the U gets close to the $\hbar\omega$, the influence of the resonance is visible. Too close to the resonance, the one-frequency assumption does not hold anymore.

The same effect appears if we decrease ω. This can be seen in figure 4.7(b) where $\hbar\omega$ is only $1.5 \cdot U$. While for $\hbar\omega = 2.75 \cdot U$ in 4.7(a), the dominating frequency had about 230 times the amplitude of the second frequency, this ratio is now down to 16. Also, as can be seen by the minimum of the sum of the pairs at the two sites being about 0.86[4] (see fig. 4.7(b)), the pair breaks with a 14 % probability at worst, invalidating the assumption that spin flip terms do not contribute.

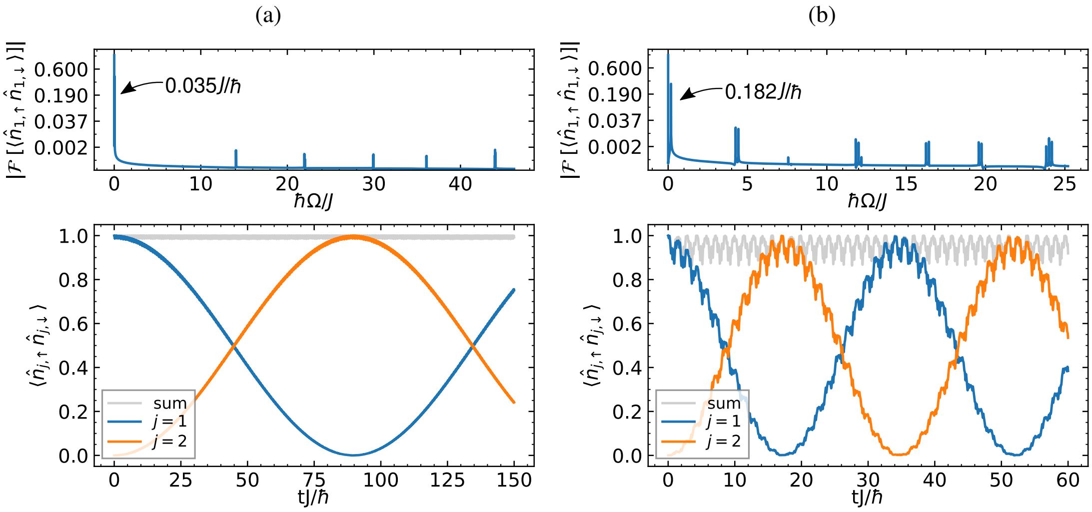
(a)

(b)

Figure 4.7: Time evolution of a particle pair initially located at $j = 1$ (lower panel) and its Fourier spectrum (upper panel) for $U = -8J$. (a) For high driving frequency $\hbar\omega = 22J$, (b) closer to the resonances for $\hbar\omega = 12J$. The arrows mark the lowest non-zero frequency $\Omega_\text{P,min}$.

We have to find the minimal ω and maximal U for which the influence of the resonance is not too big. As a compromise, we fix $\hbar\omega = 1.7 \cdot U$ and try to tune U. The resulting pair frequencies, denoted by $\Omega_\text{P,min,high}$, are visualized in figure 4.8(b). To quantitatively estimate the influence of the resonance, the minimum total number of pairs $\langle \hat{N}_\text{pair} \rangle_\text{min}$ is shown beneath.

---

[4] In other words, $\langle \hat{N}_\text{pair} \rangle_\text{min} = 0.86$.

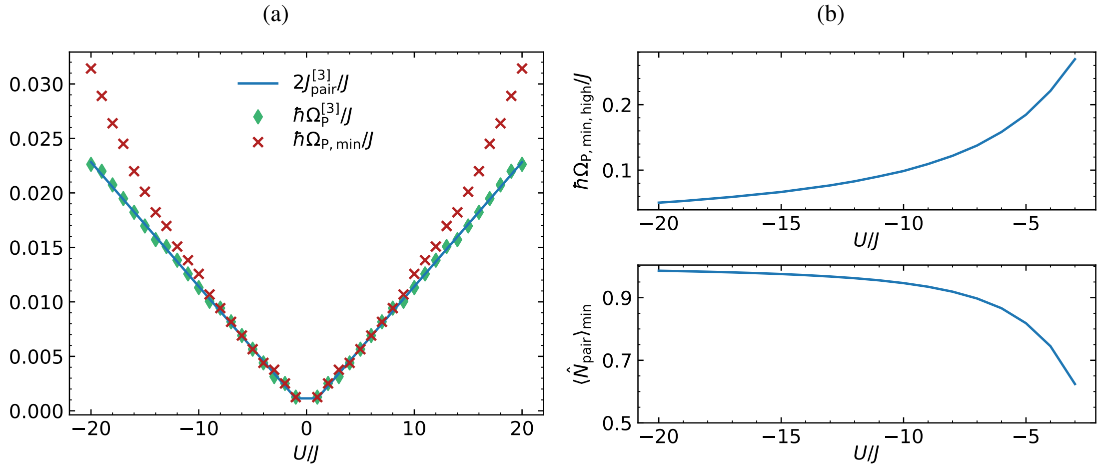
(a)

(b)

Figure 4.8: (a) Numerical $\Omega_{\mathrm{P,min}}$ and $\Omega^{[3]}_{\mathrm{P}}$ compared to an ideal model with $J_{\mathrm{pair}} = J^{[3]}_{\mathrm{pair}}$ at fixed $\hbar\omega = 40J$. Linear dependence on U in the high frequency regime. (b) Lowest non-zero pair hopping frequency $\Omega_{\mathrm{P,min,high}}$ at $\hbar\omega = 1.7 \cdot U$ and minimum probability of the pair sticking together $\langle\hat{N}_{\mathrm{pair}}\rangle_{\mathrm{min}}$.

If we demand that the pair breaks with no more than 10 % probability, i. e. $\langle\hat{N}_{\mathrm{pair}}\rangle_{\mathrm{min}} \geq 0.90$, we need to choose $U \leq -7.5$ and yield $\Omega_{\mathrm{P,min,high}} \lesssim 0.12$, corresponding to $J_{\mathrm{pair}} \lesssim 0.06$. Assuming we can tune $\kappa/\hbar\omega$ finely enough to reach $J_{\mathrm{eff}} \leq 0.25 \cdot 10^3$, this means $J_{\mathrm{pair}}/J_{\mathrm{eff}} \approx 240$. If the pair shall not break with more than 5 % probability, the ratio decreases to $J_{\mathrm{pair}}/J_{\mathrm{eff}} \approx 180$. Note that the factor 1.7 in the condition between $\hbar\omega$ and U was chosen rather arbitrarily, and as can be seen clearly in the lower plot of figure 4.8(b) the distance from $\hbar\omega \approx U$ at which the resonance is losing influence is not $1.7 \cdot U$ for all U. However, it has been found that for factors greater or lower than 1.7 the maximally achievable ratio $J_{\mathrm{pair}}/J_{\mathrm{eff}}$ only barley changes.

4.3.2 Resonance Regime

In the vicinity of the resonances, $\Omega_{\mathrm{P,min}}$ is visibly increased, but we also have to be careful because competing frequencies are involved and the pairs are breaking (cf. figures 4.3 and 4.6). Both effects are strongly visible in figure 4.9(a) which shows the time evolution of a pair at the resonance $\hbar\omega \approx |U|$ and the corresponding Fourier transform for $U = -20J$. Obviously the evolution is not governed by a single frequency. Also, since the sum of the pairs at the two sites gets as low as 0.45[5], we can infer that the pair is not sticking together but is broken up with a 55 % probability at worst.

Both issues become less pronounced in between the two highest resonances, i. e. between $\hbar\omega \approx U$ and $\hbar\omega \approx U/2$. Figure 4.9(b) shows the time evolution of a particle pair in the middle of this regime. Here, the pair only breaks up with a 14 % probability at worst. Excluding the $\Omega = 0$ contribution, there is one dominant frequency $\Omega = \Omega_{\mathrm{P,min}} = 0.293J/\hbar$. The next-highest peak in the spectrum only has about 1/16'th of the amplitude. Hence, this region between the resonances is an interesting for our purposes. If we fix $\hbar\omega = 3/4 \cdot U$, then the only remaining free parameter we can look at is U.

---

[5] $\langle\hat{N}_{\mathrm{pair}}\rangle_{\mathrm{min}} = 0.45$.

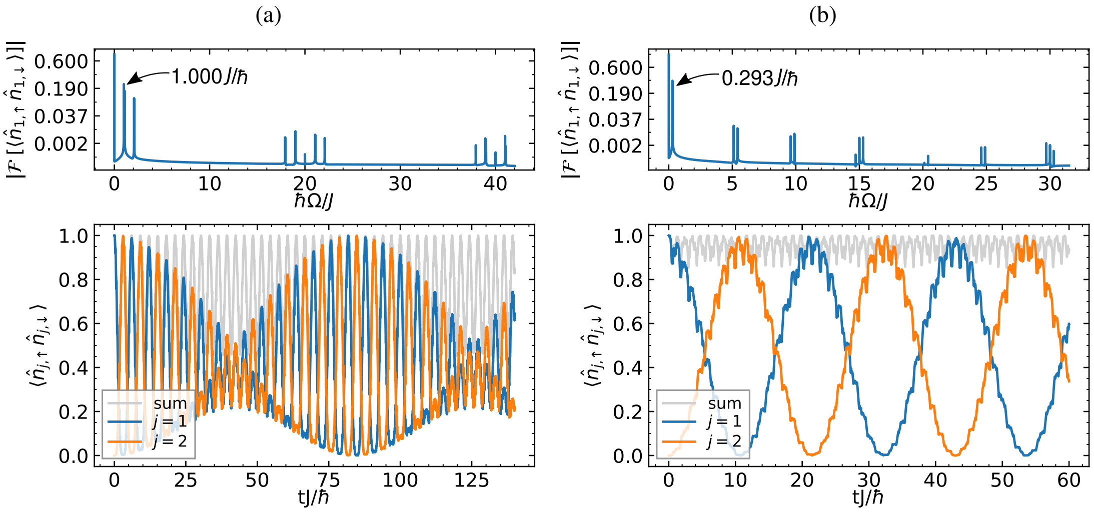

Figure 4.9: Time evolution of a particle pair, initially located at $j = 1$ and corresponding Fourier spectrum for $U = -20J$. (a) At the resonance $\hbar\omega = 20J$, (b) in between the highest two resonances, at $\hbar\omega = 15J$. The arrows mark the lowest non-zero frequency $\Omega_{\mathrm{P,min}}$.

Looking back at figures 4.3 and 4.4, $\Omega_{\mathrm{P,min}}$ in between the resonances seems to be increasing with lower U, but at the same time the other competing frequencies are gaining in magnitude. To quantify this better, figure 4.10 compares $\Omega_{\mathrm{P,min}}$ at $\hbar\omega = 0.75 \cdot U$, which we denote with $\Omega_{\mathrm{P,min,res}}$, to the minimum total pairs $\langle \hat{N}_{\mathrm{pair}} \rangle_{\mathrm{min}}$ in the evolution. Say we would impose that the pairs are breaking with no more than 10 % probability, than we would need $U \leq -25J$ yielding $\Omega_{\mathrm{P,min,res}} \lesssim 0.24J/\hbar$, corresponding to $J_{\mathrm{pair}} \lesssim 0.12J$. Assuming we can tune the single hopping down to $J_{\mathrm{eff}} \lesssim 0.25 \cdot 10^{-3}$ (cf. figure 4.2 at $\hbar\omega = 3/4 \cdot 25J$), this would mean $J_{\mathrm{pair}}/J_{\mathrm{eff}} \approx 480$. For 5 % pair breaking probability, we could reach $J_{\mathrm{pair}}/J_{\mathrm{eff}} \approx 340$. Hence, working in the resonance regime can roughly double the ratio $J_{\mathrm{pair}}/J_{\mathrm{eff}}$ compared to the high-frequency region.

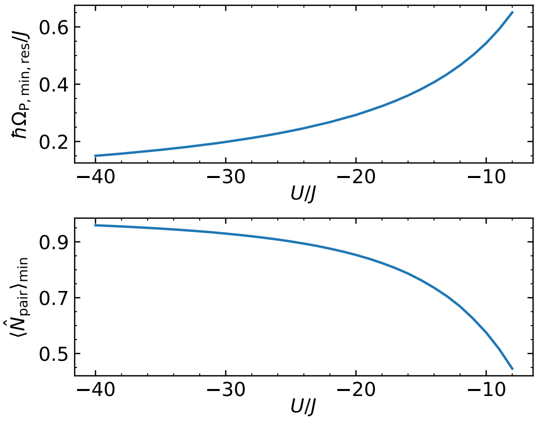

Figure 4.10: Comparison of the lowest non-zero pair hopping frequency $\Omega_{\mathrm{P,min,res}}$ to the minimum total number of pairs $\langle \hat{N}_{\mathrm{pair}} \rangle_{\mathrm{min}}$ in the time evolution in between the resonances at $\hbar\omega = 0.75 \cdot U$.

CHAPTER 5

Conclusion and Outlook

The Floquet theory of time periodic Hamiltonians could successfully be applied to the driven two-site model at hand. In the high-driving-frequency limit, the effective Hamiltonian $\hat{H}_\mathrm{F}$ was calculated and with it the time evolution of the full driven model beyond any resonances could be explained. The spectroscopical quasienergy spectra in the numerical results could be well explained by the eigenvalues of the effective Hamiltonian and exhibit a periodicity in steps of $\hbar\omega$ as predicted by the theory.

The first order approximation already enabled the suppression of the single-fermion hopping for high ω with great accuracy when choosing $\kappa/\hbar\omega \approx 2.4$. The third order extended that notably for lower frequencies and also allowed for some analysis of the pair hopping for high driving frequencies.

Two regimes of enhanced pair dynamics compared to single hopping, measured by $J_\mathrm{pair}/J_\mathrm{eff}$, could be identified. In the high-frequency region, at about $\hbar\omega = 1.7 \cdot U$, $J_\mathrm{pair}/J_\mathrm{eff}$ on the order of $2 \cdot 10^2$ could be achieved. The influence of the resonances when $\hbar\omega$ is about $0.75 \cdot U$ allows for even higher pair hopping, but has to be treated with care, since the pair is likely to break. With that in mind the resonance regime can provide an extra factor of 2 in $J_\mathrm{pair}/J_\mathrm{eff}$ compared to the high-frequency regime. The value of $J_\mathrm{pair}/J_\mathrm{eff}$ will ultimately also depend on how fine the parameters can be tuned, especially the ratio $\kappa/\hbar\omega$, which sensitively determines the single-particle hopping. Additionally, the maximal likelihood that one imposes on the pair breaking in the process plays an important role. One will thus have to make a compromise between conserving the pairs and maximizing $J_\mathrm{pair}/J_\mathrm{eff}$.

A few open secondary questions remain. First, every second repetition of the quasienergies was missing in the single-fermion evolution Fourier spectra and a reason has yet to be found. Second, the model has to be further scanned for a symmetry that explains why the observed spectra of the pair evolutions are generally independent on the sign of the interaction energy U.

In a future work, the model needs to be extended to include the whole two-leg ladder from figure 1.1. It is expected that when implementing the driving with the found parameter sets, the model proposed in [15, 16] should be approximately realized in the effective description. It can be validated numerically, whether the Majorana states appear, e. g. by looking for exponentially decaying lattice occupations from the edges of the ladder inwards [15, 16]. Experimental evidence of their existence in a realization of the full driven ladder would then have to be found.

Bibliography

[1] A. Einstein,
Quantentheorie des einatomigen idealen Gases, Erste und Zweite Abhandlung, German, Sitzungsberichte der Königlichen Preußischen Akademie der Wissenschaften (1924/1925) (cit. on p. 1).

[2] T. R. S. A. of Sciences, *The Nobel Prize in Physics 2001, Information for the Public*, `https://www.nobelprize.org/prizes/physics/2001/popular-information/`, Nobel Media AB 2020, (visited on 17/08/2020) (cit. on p. 1).

[3] P. Barmettler and C. Kollath, *Quantum gases in optical lattices*, 2013, arXiv: `1312.5772 [cond-mat.quant-gas]` (cit. on p. 1).

[4] J. Hubbard and B. H. Flowers, *Electron correlations in narrow energy bands*, Proceedings of the Royal Society of London. Series A. Mathematical and Physical Sciences **276** (1963) 238–257,
eprint: `https://royalsocietypublishing.org/doi/pdf/10.1098/rspa.1963.0204`
(cit. on pp. 1, 3).

[5] M. Greiner et al.,
Quantum phase transition from a superfluid to a Mott insulator in a gas of ultracold atoms, **415** (2002) 39–44 (cit. on p. 1).

[6] I. Bloch, J. Dalibard and W. Zwerger, *Many-body physics with ultracold gases*, Reviews of Modern Physics **80** (2008) 885–964, ISSN: 1539-0756 (cit. on p. 1).

[7] I. Bloch, J. Dalibard and S. Nascimbène, *Quantum simulations with ultracold quantum gases*, Nature Physics **8** (2012) 267–276 (cit. on p. 1).

[8] A. Eckardt and E. Anisimovas, *High-frequency approximation for periodically driven quantum systems from a Floquet-space perspective*, New Journal of Physics **17** (2015) 093039 (cit. on pp. 1, 8, 11, 12, 15).

[9] A. Eckardt, *Colloquium: Atomic quantum gases in periodically driven optical lattices*, Rev. Mod. Phys. **89** (1 2017) 011004 (cit. on pp. 1, 10).

[10] F. Wilczek, *Majorana returns*, Nature Physics **5** (2009) 614–618 (cit. on p. 1).

[11] E. Majorana, *Teoria simmetrica dell'elettrone e del positrone*, Il Nuovo Cimento **14** (1937) 171–184 (cit. on p. 1).

[12] J. Alicea, *New directions in the pursuit of Majorana fermions in solid state systems*, Reports on Progress in Physics **75** (2012) 076501 (cit. on pp. 1, 2).

[13] M. Leijnse and K. Flensberg,
Introduction to topological superconductivity and Majorana fermions,
Semiconductor Science and Technology **27** (2012) 124003 (cit. on p. 2).

[14] V. Mourik et al.,
Signatures of Majorana Fermions in Hybrid Superconductor-Semiconductor Nanowire Devices,
Science **336** (2012) 1003–1007, ISSN: 0036-8075,
eprint: `https://science.sciencemag.org/content/336/6084/1003.full.pdf`
(cit. on p. 2).

[15] F. Iemini et al.,
Localized Majorana-Like Modes in a Number-Conserving Setting: An Exactly Solvable Model,
Phys. Rev. Lett. **115** (15 2015) 156402 (cit. on pp. 2, 29, 33).

[16] N. Lang and H. P. Büchler, *Topological states in a microscopic model of interacting fermions*,
Phys. Rev. B **92** (4 2015) 041118 (cit. on pp. 2, 29, 33).

[17] M. Fisher et al., *Boson localization and the superfluid-insulator transition*,
Physical review. B, Condensed matter **40** (1989) 546–570 (cit. on p. 6).

[18] F. Bloch, *Über die Quantenmechanik der Elektronen in Kristallgittern*, German,
Zeitschrift fur Physik **52** (1929) 555–600 (cit. on p. 7).

[19] N. Ashcroft and N. Mermin, *Solid State Physics*, HRW international editions,
Saunders College, 1976, ISBN: 9780030839931 (cit. on pp. 7, 8).

[20] G. Floquet, *Sur les équations différentielles linéaires à coefficients périodiques*, French,
Annales scientifiques de l'École Normale Supérieure **2e série, 12** (1883) 47–88 (cit. on p. 7).

[21] M. Holthaus,
Floquet engineering with quasienergy bands of periodically driven optical lattices,
Journal of Physics B: Atomic, Molecular and Optical Physics **49** (2015) 013001
(cit. on pp. 8, 9, 11, 12).

[22] M. Bukov, L. D'Alessio and A. Polkovnikov, *Universal high-frequency behavior of periodically driven systems: from dynamical stabilization to Floquet engineering*,
Advances in Physics **64** (2015) 139–226,
eprint: `https://doi.org/10.1080/00018732.2015.1055918` (cit. on p. 11).

[23] M. Langemeyer and M. Holthaus, *Energy flow in periodic thermodynamics*,
Phys. Rev. E **89** (1 2014) 012101 (cit. on p. 12).

[24] S. Rahav, I. Gilary and S. Fishman, *Effective Hamiltonians for periodically driven systems*,
Phys. Rev. A **68** (1 2003) 013820 (cit. on p. 12).

[25] J. J. Sakurai and J. Napolitano, *Modern Quantum Mechanics*, 2nd ed.,
Cambridge University Press, 2017, ISBN: 9781108422413 (cit. on p. 15).

APPENDIX A

Matrix Expressions for the Hamiltonians and Density Oscillations in the High-Frequency Limit

Single Fermion $\mathcal{H}^{(1,+1/2)}$ For the case of a single fermion, we can without loss of generality choose this fermion to have spin up. A suitable basis for the two-site model can then be chosen as $\{|1000\rangle, |0010\rangle\}$, denoted by $|n_{1,\uparrow} n_{1,\downarrow} n_{2,\uparrow} n_{2,\downarrow}\rangle$ for $\mathcal{H}^{(1,+1/2)}$. In this basis, the full driven model $\hat{H}(t)$ given by equation 3.2, can be written as

$$\hat{H}(t) = \hat{H}_\mathrm{S} + \hat{V}(t) \doteq \begin{pmatrix} 0 & -J \\ -J & 0 \end{pmatrix} + \begin{pmatrix} V(t) & 0 \\ 0 & V(t) \end{pmatrix} \quad \text{, with } V(t) = \frac{\kappa}{2}\sin(\omega t)\,,$$

where we have used the notation " $\doteq$ " to indicate "is represented by". For the effective models in the high frequency approximation, derived in section 3.2, we find

$$\hat{H}_\mathrm{F}^{[1]} \doteq \begin{pmatrix} 0 & -J_\mathrm{eff}^{[1]} \\ -J_\mathrm{eff}^{[1]} & 0 \end{pmatrix} \quad \text{and} \quad \hat{H}_\mathrm{F}^{[3]} \doteq \begin{pmatrix} 0 & -J_\mathrm{eff}^{[3]} \\ -J_\mathrm{eff}^{[3]} & 0 \end{pmatrix}\,,$$

in perfect analogy to the static single-fermion model in section 2.1.1. There, we found that when starting with a single fermion on one site, evolving this system with the static two-site Hubbard Hamiltonian $\hat{H}_\mathrm{S}$ would make the particle oscillate back and forth between the two sites according to equation 2.7. We can immediately apply this result to the effective Hamiltonian in first and third order, since in the restricted case of a single fermion, the effective model just resembles the static model, only with a modified hopping amplitude J_eff. The effective frequencies of this oscillation are given by $\Omega_\mathrm{S}^{[1/3]} = 2J_\mathrm{eff}^{[1/3]}/\hbar$.

Two Fermions $\mathcal{H}^{(2,0)}$ In the case of two fermions with opposite spins, i. e. in $\mathcal{H}^{(2,0)}$, we choose the basis $\{|1001\rangle, |1100\rangle, |0110\rangle, |0011\rangle\}$. Then,

$$\hat{H}(t) = \hat{H}_\mathrm{S} + \hat{V}(t) \doteq \begin{pmatrix} 0 & -J & 0 & -J \\ -J & U & J & 0 \\ 0 & J & 0 & J \\ -J & 0 & J & U \end{pmatrix} + V(t) \cdot \begin{pmatrix} 0 & 0 & 0 & 0 \\ 0 & -2 & 0 & 0 \\ 0 & 0 & 0 & 0 \\ 0 & 0 & 0 & 2 \end{pmatrix}, \tag{A.1}$$

and for the effective models

$$\hat{H}_{\mathrm{F}}^{[1]} \doteq \begin{pmatrix} 0 & -J_{\mathrm{eff}}^{[1]} & 0 & -J_{\mathrm{eff}}^{[1]} \\ -J_{\mathrm{eff}}^{[1]} & U & J_{\mathrm{eff}}^{[1]} & 0 \\ 0 & J_{\mathrm{eff}}^{[1]} & 0 & J_{\mathrm{eff}}^{[1]} \\ -J_{\mathrm{eff}}^{[1]} & 0 & J_{\mathrm{eff}}^{[1]} & U \end{pmatrix} \quad \text{and} \quad \hat{H}_{\mathrm{F}}^{[3]} \doteq \begin{pmatrix} W_i & -J_{\mathrm{eff}}^{[3]} & -W_i & -J_{\mathrm{eff}}^{[3]} \\ -J_{\mathrm{eff}}^{[3]} & U - W_i & J_{\mathrm{eff}}^{[3]} & J_{\mathrm{pair}}^{[3]} \\ -W_i & J_{\mathrm{eff}}^{[3]} & W_i & J_{\mathrm{eff}}^{[3]} \\ -J_{\mathrm{eff}}^{[3]} & J_{\mathrm{pair}}^{[3]} & J_{\mathrm{eff}}^{[3]} & U - W_i \end{pmatrix} .$$

Starting with a pair of fermions on site $j = 1$ in an idealized model, cf. section 4.1, we found a similar oscillation to the single-particle case, where the pair was hopping together in unity. The effective Hamiltonian includes additional terms that deviate from this idealized model and destroy the single frequency oscillations. Yet, it is useful to study the occurring multiple frequency oscillations. Defining

$$\langle \hat{n}_{1,\uparrow}\hat{n}_{1,\downarrow}\rangle_{\mathrm{F}}^{[n]}(t) := \langle 1100|\exp\left(i\frac{\hat{H}_{\mathrm{F}}^{[n]}t}{\hbar}\right)\cdot \hat{n}_{1,\uparrow}\hat{n}_{1,\downarrow}\cdot\exp\left(-i\frac{\hat{H}_{\mathrm{F}}^{[n]}t}{\hbar}\right)|0011\rangle \ ,$$

we find

$$\begin{aligned}\langle \hat{n}_{1,\uparrow}\hat{n}_{1,\downarrow}\rangle_{\mathrm{F}}^{[1]} =& \frac{1}{2}\left[\frac{U\sin\left(\frac{tU}{2}\right)\sin\left(\frac{1}{2}t\sqrt{16J_{\mathrm{eff}}^2+U^2}\right)}{\sqrt{16J_{\mathrm{eff}}^2+U^2}} + \frac{4J_{\mathrm{eff}}^2\left(\cos\left(t\sqrt{16J_{\mathrm{eff}}^2+U^2}\right)-1\right)}{16J_{\mathrm{eff}}^2+U^2}\right.\\ &\left. +\cos\left(\frac{tU}{2}\right)\cos\left(\frac{1}{2}t\sqrt{16J_{\mathrm{eff}}^2+U^2}\right)+1\right]\end{aligned} \tag{A.2}$$

to first order and

$$\begin{aligned}\langle \hat{n}_{1,\uparrow}\hat{n}_{1,\downarrow}\rangle_{\mathrm{F}}^{[3]} =& \frac{1}{16\left(16J_{\mathrm{eff}}^2+\left(-3W_{\mathrm{i}}+J_{\mathrm{pair}}+U\right)^2\right)}\\ &\cdot\left\{\left[\left(\sqrt{16J_{\mathrm{eff}}^2+\left(-3W_{\mathrm{i}}+J_{\mathrm{pair}}+U\right)^2}+3W_{\mathrm{i}}-J_{\mathrm{pair}}-U\right)\right.\right.\\ &\quad\cdot\exp\left(-\frac{1}{2}it\left(-\sqrt{16J_{\mathrm{eff}}^2+\left(-3W_{\mathrm{i}}+J_{\mathrm{pair}}+U\right)^2}+W_{\mathrm{i}}+J_{\mathrm{pair}}+U\right)\right)\\ &+\left(\sqrt{16J_{\mathrm{eff}}^2+\left(-3W_{\mathrm{i}}+J_{\mathrm{pair}}+U\right)^2}-3W_{\mathrm{i}}+J_{\mathrm{pair}}+U\right)\\ &\quad\cdot\exp\left(-\frac{1}{2}it\left(\sqrt{16J_{\mathrm{eff}}^2+\left(-3W_{\mathrm{i}}+J_{\mathrm{pair}}+U\right)^2}+W_{\mathrm{i}}+J_{\mathrm{pair}}+U\right)\right)\\ &\left.+2e^{-it\left(-W_{\mathrm{i}}-J_{\mathrm{pair}}+U\right)}\sqrt{16J_{\mathrm{eff}}^2+\left(-3W_{\mathrm{i}}+J_{\mathrm{pair}}+U\right)^2}\right]\end{aligned} \tag{A.3}$$

$$
\begin{aligned}
&\cdot\Bigg[\left(\sqrt{16J_{\text{eff}}^2+\left(-3W_{\text{i}}+J_{\text{pair}}+U\right)^2}+3W_{\text{i}}-J_{\text{pair}}-U\right)\\
&\qquad\cdot\exp\left(\frac{1}{2}it\left(-\sqrt{16J_{\text{eff}}^2+\left(-3W_{\text{i}}+J_{\text{pair}}+U\right)^2}+W_{\text{i}}+J_{\text{pair}}+U\right)\right)\\
&+\left(\sqrt{16J_{\text{eff}}^2+\left(-3W_{\text{i}}+J_{\text{pair}}+U\right)^2}-3W_{\text{i}}+J_{\text{pair}}+U\right)\\
&\qquad\cdot\exp\left(\frac{1}{2}it\left(\sqrt{16J_{\text{eff}}^2+\left(-3W_{\text{i}}+J_{\text{pair}}+U\right)^2}+W_{\text{i}}+J_{\text{pair}}+U\right)\right)\\
&+2e^{it\left(-W_{\text{i}}-J_{\text{pair}}+U\right)}\sqrt{16J_{\text{eff}}^2+\left(-3W_{\text{i}}+J_{\text{pair}}+U\right)^2}\,\Bigg]\Bigg]\Bigg\}
\end{aligned}
\tag{A.3}
$$

to third order. Note that $\hbar$ is set to 1 and the superscripts $^{[n]}$ for the order of the effective hopping and pair hopping amplitudes J_{eff} and J_{pair} are suppressed in both equations A.2 and A.3 in an attempt to increase readability. Also, even though equation A.3 includes complex exponentials, the overall value $\langle\hat{n}_{1,\uparrow}\hat{n}_{1,\downarrow}\rangle_{\text{F}}^{[3]}$ is real, as it should be.

List of Figures
